Chapter 6

Results for polar coronal holes and polar plumes

This Chapter is organized as follows. First, Section 6.1 presents examples of on-disc observations of polar holes, to show the similarities between the Elephant's Trunk equatorial coronal hole and the polar holes. Examples of off-limb coronal hole observations can then be found in Section 6.2, where plume and inter-plume regions are treated separatedly, in order to establish the contribution of plume material in the determination of the coronal hole plasma parameters. Examples of how off-limb coronal hole observations can be affected by background diffuse emission, are also given in Section 6.2. Section 6.3 then presents results from two on-disc observations of polar plumes, and shows the similarities with the Elephant's Trunk low-latitude plume presented in Chapter 5, with a CDS-EIT comparison.

As for the results presented in Chapter 5, the *Arnaud and Rothenflug* (1985) ionization equilibrium for all the ions has been adopted, together with the calculations of *Landini and Monsignori Fossi* (1991) for the minor elements. CHIANTI v.2 (*Landi et al.*, 1999b), together with the recent Fe XIV calculations (*Storey et al.*, 1999) and Mg IX calculations (P. Young, 1999, priv. comm.) have been used. For those ions that are not present in the CHIANTI database, the Arcetri spectral code (AC, see, e.g. *Landi and Landini*, 1998a) was used. The continuum emission has been calculated by the method described in *Landi et al.* (1999b).

6.1 On-disc observations of polar holes

All the polar coronal hole observations analysed by the author have shown the same type of characteristics as the equatorial hole (Elephant's trunk), although some spatial and temporal variations of all the parameters have been observed. An example of an observation containing various structures is given here.

The October 10th 1997 observations of a polar coronal hole region, with a plume, quiet sun, and a bright point

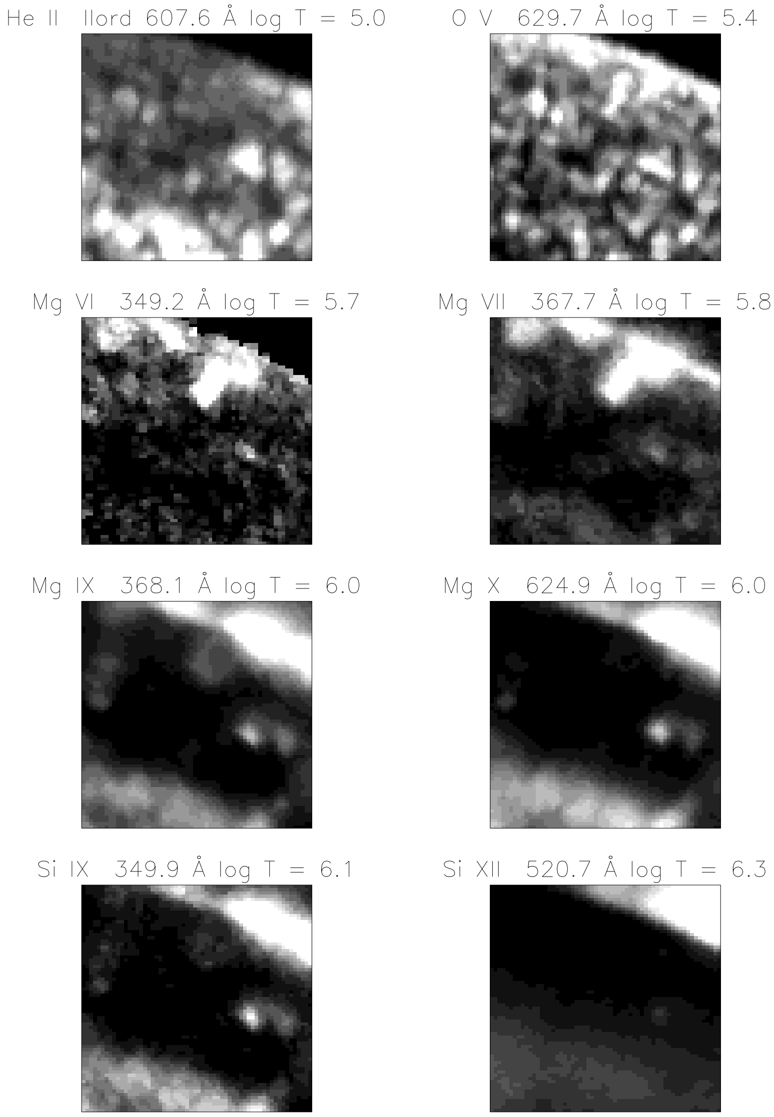

Figure 6.1: *Monochromatic images – 10th October 1997.*

On 1997 October 10, a NW region of the solar corona was rastered three times with NIS (in 2 hours). The spectra have been averaged, to increase the signal-to-noise (temporal variations were small). Figure 6.1 shows some monochromatic images. This area contains a quiet sun region in the lower part, a bright polar plume (visible in Mg VI-IX lines) and a bright point (visible in all lines). This observation is typical of those made in 1997. The main difference compared to the 1996 observations, was an increased diffuse emission in all the higher-temperature (above a million degrees) lines, even apparent in coronal hole regions.

Intensity ratio images were formed and are shown in Figure 6.2. They show temperatures and densities (at both coronal and transition region heights).

Densities and temperatures have been derived from spatially-averaged spectra of various areas (Figure 6.3). The results are presented in Table 6.1. The coronal hole and quiet sun temperatures and densities are similar to the values deduced from the August 1996 observations. Note from Figure 6.2 and Table 6.1:

- a decrease in the density inside the coronal hole region, both at coronal (Si IX) and transition region (O IV) heights. At coronal heights, densities decrease from $N_e \simeq$ 4x10^8 cm^{-3} to $N_e \simeq$ 2x10^8 cm^{-3}, in the coronal holes, i.e. a factor of two lower.
- In the lower transition region (O IV), the averaged coronal hole density is $N_e \simeq$ 1x10^{10} cm^{-3} in the network, with consistently higher values (by a factor of 2) in the cell-centre areas. In the quiet sun areas, the densities in the network and cell-centre regions are both a factor of 2 higher than in the coronal hole region.
- Isothermal temperature maps show coronal holes having lower temperatures than quiet sun areas. Values in the quiet sun are $T \simeq$ 9-11 x10^5 K, while values in the coronal hole region are in the range $T \simeq$ 8.4-8.9 x10^5 K.
- The bright point shows a higher coronal density $N_e \simeq$ 6x10^8 cm^{-3} (with even higher values from Fe XIII) and similar temperatures to the quiet sun.
- The plume is not visible in Si IX and the data yield average densities similar to the coronal hole, but marked lower temperature. At upper transition region heights, the Mg VII intensity is very high, and it is possible to deduce a plume density $N_e = 1.1 \pm 0.2$x10^9 cm^{-3} with small uncertainties.
- The plume had even lower temperatures than the ambient coronal hole regions, with $T \simeq$ 7.9 x10^5 K.

Figure 6.4 shows a coronal 'pressure' image, created by multiplying the densities obtained from the intensity ratio image of Si IX, with the temperatures obtained from the Mg X/Mg IX intensity ratio. The difference between coronal hole regions and the quiet sun is obviously highlighted. Similarly, pressure maps in the transition region, show the large differences in pressure between the various regions.

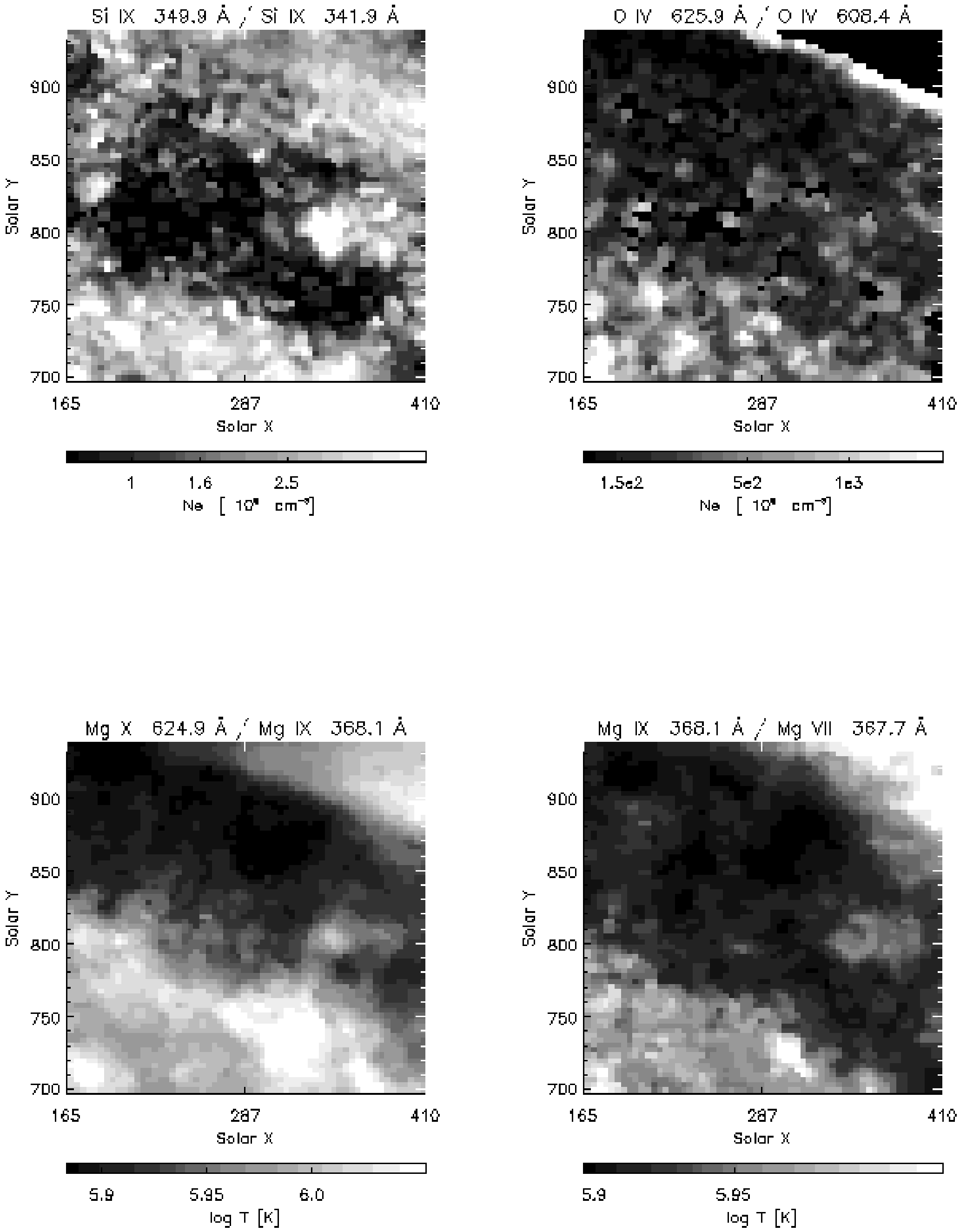

Figure 6.2: *Intensity ratio images – October 10th 1997.*

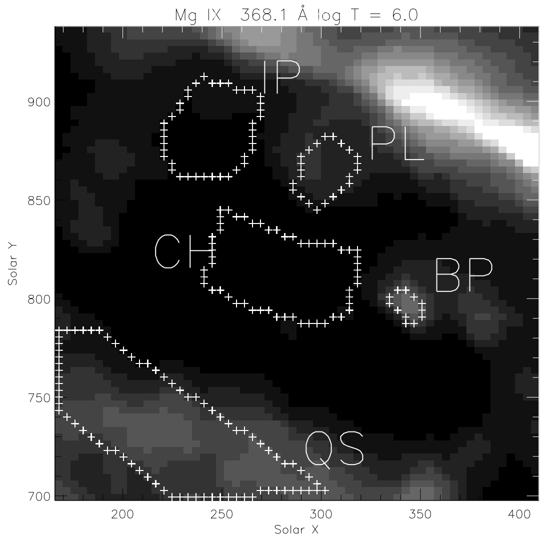

Figure 6.3: *Selected areas: plume (PL); inter-plume (IP); coronal hole (CH); quiet sun (QS); bright point (BP). – October 10th 1997.*

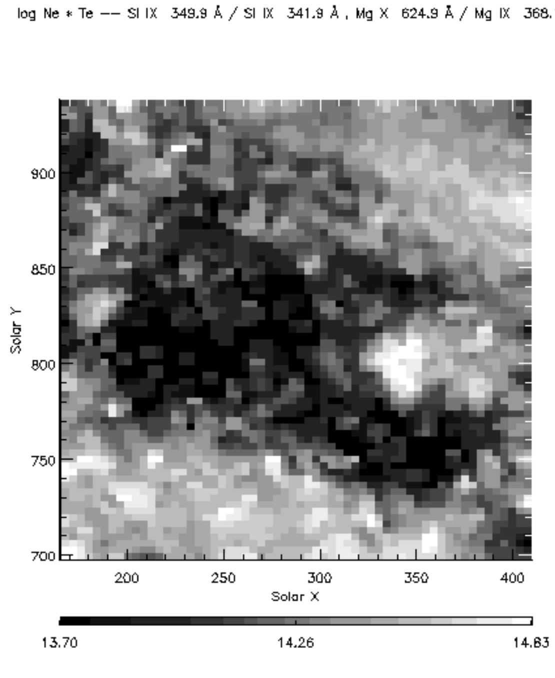

Figure 6.4: *A pressure image – October 10th 1997.*

Table 6.1: *Table of parameters deduced from the 10th October 1997 averaged spectra of the selected regions. The coronal hole (CH) and quiet sun (QS) regions have been subdivided into network (Net) and cell centres (CC).*

	plume	inter-plume	CH Net	CH CC	QS Net	QS CC	BP
N_e (O IV 625.8/554.5 Å)	$0.6\pm0.1\ 10^{10}$	$0.7\pm0.1\ 10^{10}$	$0.7\pm0.2\ 10^{10}$	$1.2\pm0.5\ 10^{10}$	$1.5\pm0.2\ 10^{10}$	$2.7\pm0.2\ 10^{10}$	$1.6\pm0.3\ 10^{10}$
N_e (O IV 625.8/608.4 Å)	$0.7\pm0.1\ 10^{10}$	$0.8\pm0.1\ 10^{10}$	$0.7\pm0.1\ 10^{10}$	$1.5\pm0.5\ 10^{10}$	$1.6\pm0.1\ 10^{10}$	$2.5\pm0.3\ 10^{10}$	$1.9\pm0.4\ 10^{10}$
N_e (Mg VII 319.0 / 367.7 Å)	$1.1\pm0.2\ 10^{9}$	$7\pm3\ 10^{8}$	$9\pm6\ 10^{8}$	$3.3\pm1\ 10^{8}$	$1.0\pm0.3\ 10^{9}$	$8\pm3\ 10^{8}$	$9\pm5\ 10^{8}$
N_e (Si IX 349.9/341.9 Å)	$2.\pm0.8\ 10^{8}$	$1.9\pm0.6\ 10^{8}$	$1.9\pm0.7\ 10^{8}$	$2.3\pm1\ 10^{8}$	$4.\pm0.6\ 10^{8}$	$3.6\pm0.5\ 10^{8}$	$6\pm3\ 10^{8}$
N_e (Fe XIII 320.8 / 348.183 Å)	$6\pm6\ 10^{8}$	$2\pm2\ 10^{9}$	$4\pm3\ 10^{8}$	$8.4\pm5\ 10^{8}$	$6.7\pm0.8\ 10^{8}$	$5.3\pm1\ 10^{8}$	$2.1\pm0.8\ 10^{9}$
T_e (Mg X 624.9 Å/ Mg IX 368 Å)	$8.1\pm0.1\ 10^{5}$	$8.6\pm0.1\ 10^{5}$	$8.8\pm0.1\ 10^{5}$	$8.9\pm0.1\ 10^{5}$	$1.1\pm0.1\ 10^{6}$	$1.1\pm0.1\ 10^{6}$	$9.8\pm0.1\ 10^{5}$
T_e (Mg IX 368 Å/ Mg VII 367.7 Å)	$7.7\pm0.1\ 10^{5}$	$8.1\pm0.1\ 10^{5}$	$8.4\pm0.1\ 10^{5}$	$8.4\pm0.1\ 10^{5}$	$9.0\pm0.1\ 10^{5}$	$9.1\pm0.1\ 10^{5}$	$8.6\pm0.1\ 10^{5}$

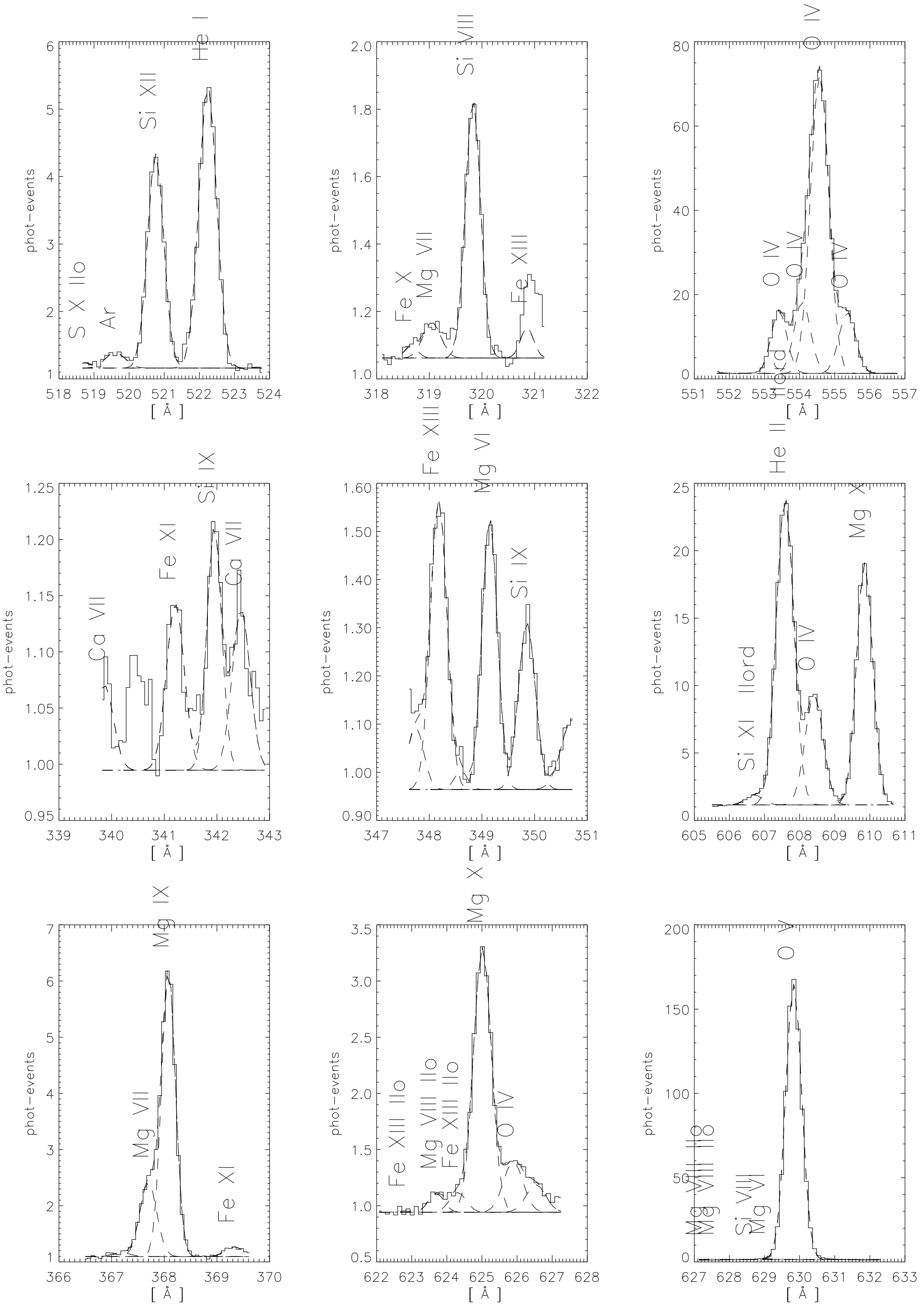

Figure 6.5: *Averaged spectra of the network coronal hole region – October 10th 1997. Note how high-temperature lines such as Fe XIII and Si XII are now bright, compared to the 1996 observations of the Elephant's Trunk (see, e.g., Figure 5.9).*

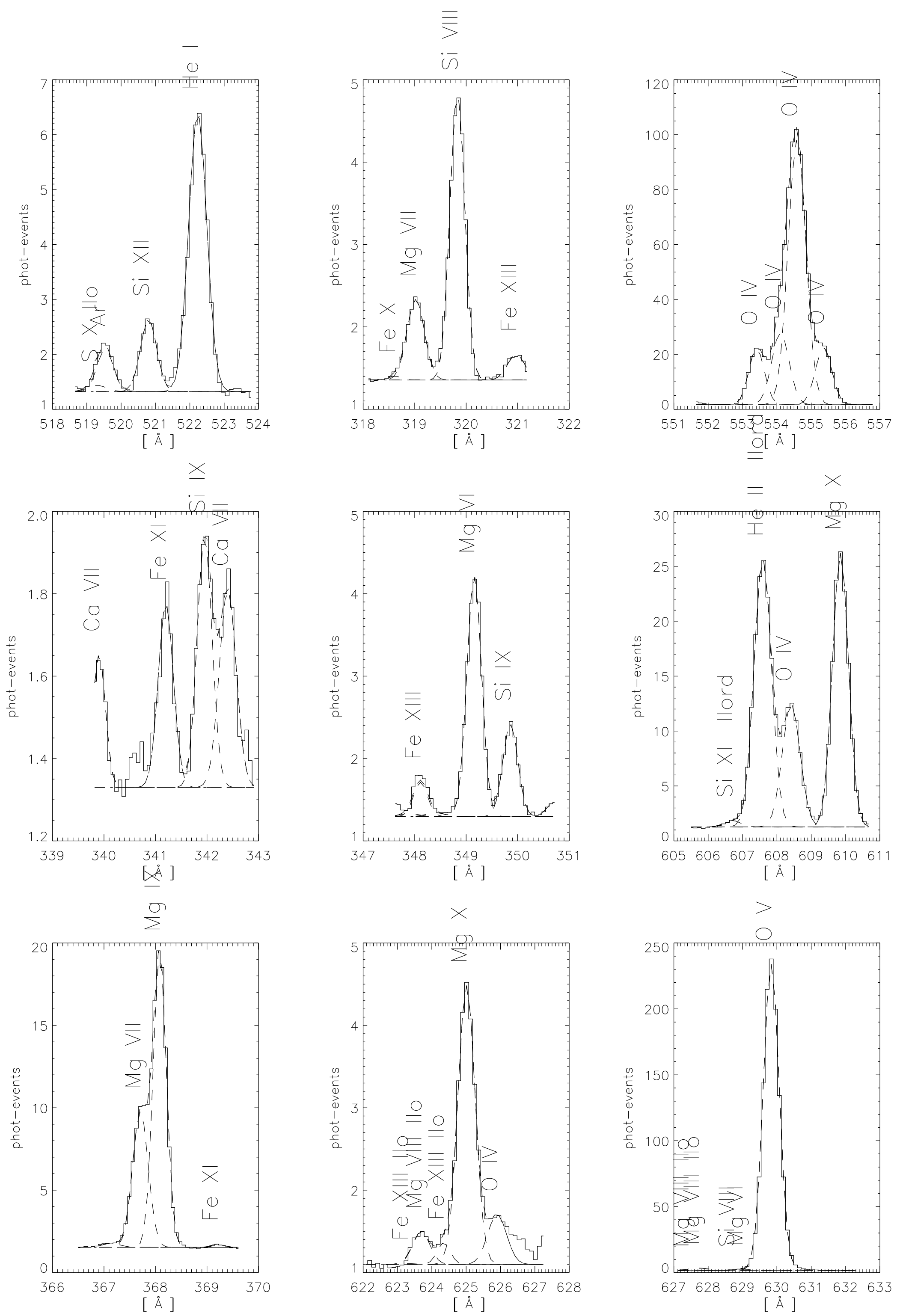

Figure 6.6: *Averaged spectra of the plume region – October 10th 1997. Note the similarities with the Elephant's Trunk plume, in the bright transition region lines emitted by Mg VI, Mg VII and Ca VII.*

Observations of the quiet sun – coronal hole boundary

During 1996 and 1997, many observations of quiet sun – coronal hole boundaries were performed, mainly near the meridian on some equatorward extensions of one of the polar holes. In general terms, all observations produced the same type of result for this boundary that has already been described for the Elephant's Trunk. The boundary is evident in the He lines and in the coronal lines, and in terms of physical parameters is not sharp, but shows a slow decrease of electron density and temperature toward the coronal hole regions, where the pressure is lower. Small-scale inhomogeneities in all the derived parameters have been observed.

The relative element abundances appear to vary slightly, with values similar to the photospheric ones. There is a tendency to have a small FIP effect related to the supergranular pattern, with a difference between the coronal hole and the quiet sun regions, although as already shown some of these differences can be explained in terms of differential emission measure variations. DEM analyses on the polar regions have been done, but they have the drawback of suffering from some projection effects and the derived element abundances may not be correct. The near-disc-centre observations are to be preferred for DEM and abundance analysis. In fact, in the polar observations, if regions in the network are selected from the intensity of a transition region line, then the corresponding area at coronal heights might have some mixing of plasma that instead originated from nearby cell-centre regions, close to the line of sight. However, the observed abundance variations have been seen in all the NIS rasters analysed, independent of the angle of the line of sight to the radial direction.

Figure 6.7 shows as an example a series of monochromatic images of a coronal hole boundary observed on 1997 October 14. Six repetitions of the NIS full wavelength raster UCLAN_N2 have been analysed and averaged, to increase the signal-to-noise. The boundary is evident in the He and coronal lines.

Figure 6.8 shows some intensity ratio images, illustrating the decrease in density and temperature, and possible element abundance variations, in the region of the coronal hole boundary.

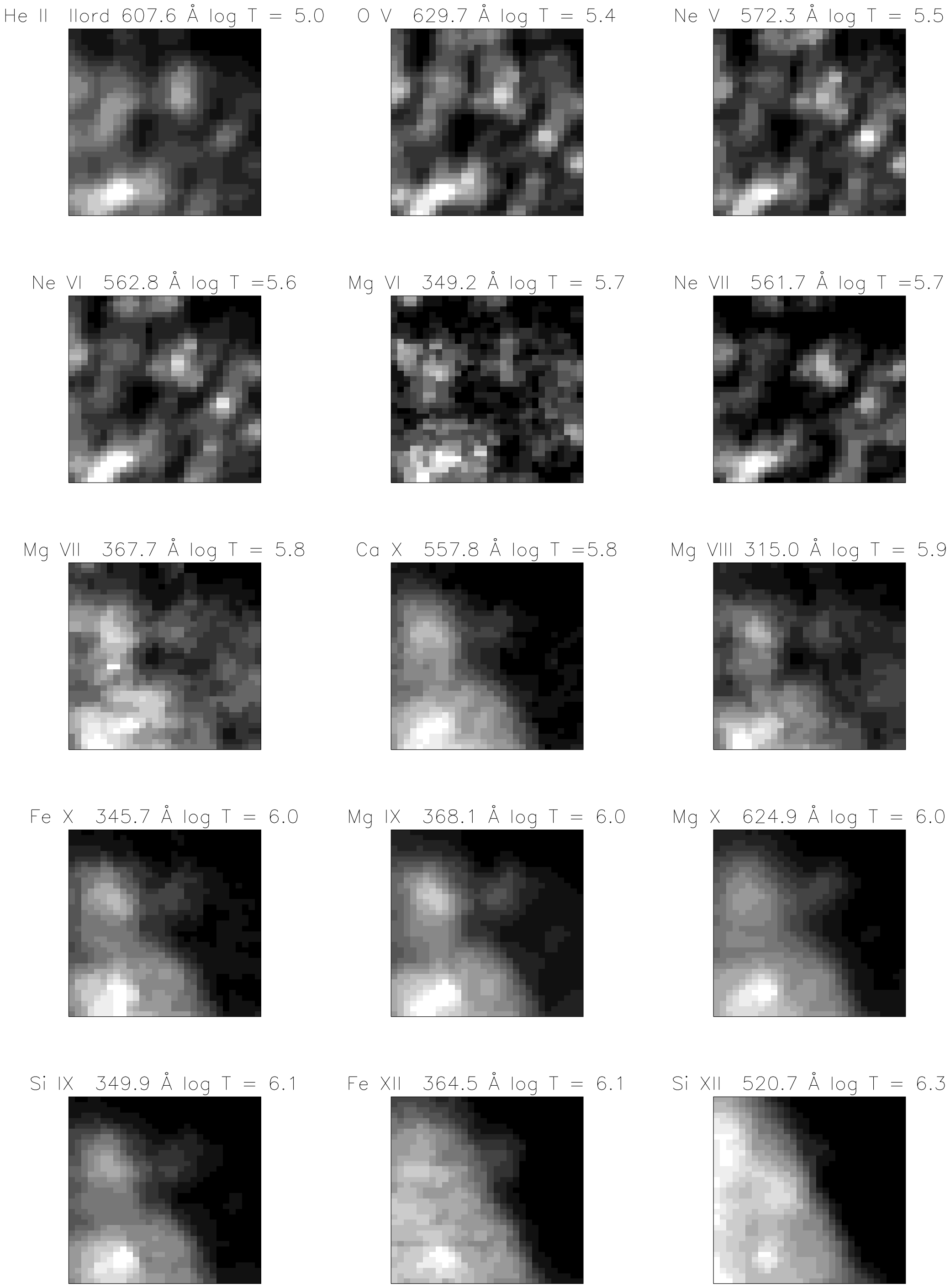

Figure 6.7: – *Monochromatic images of a boundary – 14th October 1997.*

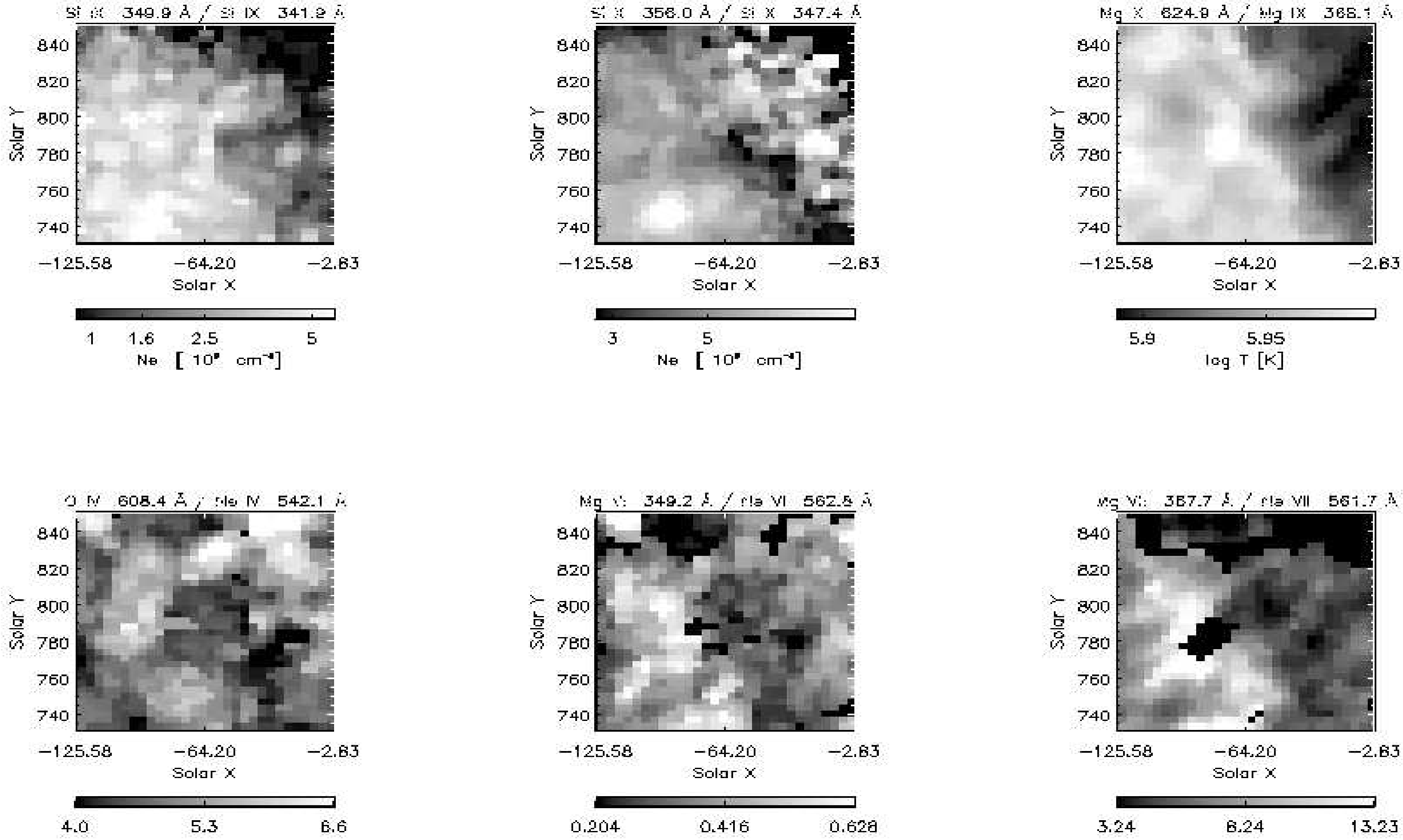

Figure 6.8: – *Ratio images of a boundary – 14th October 1997.*

6.2 Off-limb observations of polar holes and plumes

The off-limb coronal hole observations of the 12th of September 1997

On 1997 October 12 between 16:01 and 18:28 UT, CDS observed the north polar hole with the CORO24W study, as part of a synoptic program devised by A. Fludra. The CORO24W study extracts only a limited number of lines. Figure 6.9 displays a mosaic of monochromatic images of the observed region. These show the presence of two plumes, one on each side of the meridian, most visible in the upper transition region lines (excluding the Ne lines).

Prior to these studies, six repetitions of the NISAT_S5 study, starting at 08:55 UT, were performed (see Figure 4.9). This observation represents the longest off-limb inter-plume observation by CDS, since it lasted for almost 7 hours. An analysis of the single observations showed very little variations in time. The six observations were therefore subsequently averaged, to increase the signal-to-noise. Furthermore, an inter-plume area of 24″in Solar X (centred at Solar X = -7) was selected for the average, to produce radial profiles. This averaging along Solar Y, using increasing spatial areas with radial distance, was also applied to the spectra before fitting and deriving the line intensities. Figure 6.11 (top four rows) shows intensity profiles of some selected lines. With all the averaging performed, the signal was of acceptable strength for most lines. Two areas in the CORO24W study were selected for comparisons (these are shown in Figure 6.10): 1) the brightest plume region; and 2) an inter-plume region eastward of the eastern plume. Figure 6.11 also shows the radial profiles of the intensities of some lines in the plume region. Note how the chromospheric and transition region intensities rapidly fall off-limb, showing how little stray light was present, and how lines that are formed at different temperatures have different profiles.

Figures 6.12 and 6.13 (upper plots) present densities and isothermal temperatures as derived from some of the line ratios where the signal was acceptable. These results extend out to R= 1.2 $R_\odot$ those presented by *Fludra et al.* (1999a) and (1999b), that in the coronal hole regions extended out to 1.1 $R_\odot$, and moreover distinguish between plume and inter-plume regions. Note that:

- very low values of $N_e \simeq 5\text{x}10^7$ cm^{-3} are reached at 1.2 $R_\odot$; and
- the densities derived from Si IX are slightly higher (at lower heights) than those derived from Mg VIII. This difference could be the signature of the photoionization processes that have been neglected in calculating the densities (see discussion in Chapter 2). However, Si X densities in the same region are even higher.

The differences in the derived densities could be real, and not due to having neglected photoionization in the level population calculations. In fact, the plasma that emits these ions is not co-spatial. Indeed, evidence from deriving temperatures from line ratios suggest that the plasma is not isothermal, as Figure 6.13 shows. While temperatures from the Mg X / Mg IX ratio show increasing values between $T \simeq 8\text{x}10^5$ K and $T \simeq 9\text{x}10^5$ K, other ratios show different values, except for the Mg IX / Mg VII ratio near the base of the plume. Using ratios of higher-temperature ions, such as Si XII / Si XI and Fe XIII /Fe XII, the temperature appears to rapidly increase just off-limb, and then decrease. This is due to some diffuse background emission at temperatures above a million degrees, which is present along the line of sight , as shown with a DEM analysis below.

A rectangular area across the plumes was selected between 1.04 and 1.06 $R_{\odot}$, and spectra were averaged along the Solar Y direction. Figure 6.14 shows some of the intensity profiles across the plumes, together with densities and temperatures. The higher-temperature lines (e.g. Fe XIII, Fe XVI) show the presence of diffuse hot plasma in the background, in particular in the western side of the observations. The transition region lines (Mg VII, Ca X in particular) show the profiles of the two plumes. Note how these profiles are different in all the lines examined, and how complex the emission is. Densities derived from Si IX show slightly higher values in the plume regions, while temperatures derived from Mg IX/Mg VII indicate lower values ($T \simeq 8.5\text{x}10^5$ K) in the region of the brightest plume. The temperature as derived from Mg X/Mg IX agrees only in this plume region, indicating isothermal plasma. In Figure 6.13 (bottom) it can be seen that the plume is only strictly isothermal between 1.02 and 1.06 $R_{\odot}$. Temperatures derived from Fe XII/Fe X are higher, again because most of the Fe XII emission is not from the plume, but from the background and foreground regions.

A more complete analysis in which the plume and background emission are separated is deferred for future work, but a DEM analysis on an off-limb inter-plume region is presented here, because it helps to assess the contamination from hot plasma in the coronal hole region. This region is indicated in Figure 6.10. It is far from the region where there is obvious contamination from hot plasma (see again Figure 6.14).

A constant density $N_{\rm e} = 1\text{x}10^8$ cm^{-3} was assumed, with the *Arnaud and Rothenflug* (1985) ionization equilibrium, photospheric abundances, and CHIANTI v.2 data. Figure 6.15 shows the result. The peak of the DEM is at $T = 9.5\text{x}10^5$ K, a value close to that derived from the Mg IX/Mg VII ratio (Figure 6.13, middle and Figure 6.14, bottom). However, the plasma distribution along the line of sight is evidently not isothermal, due to the high-temperature plasma in the background that produces significant emission measures above a million degrees.

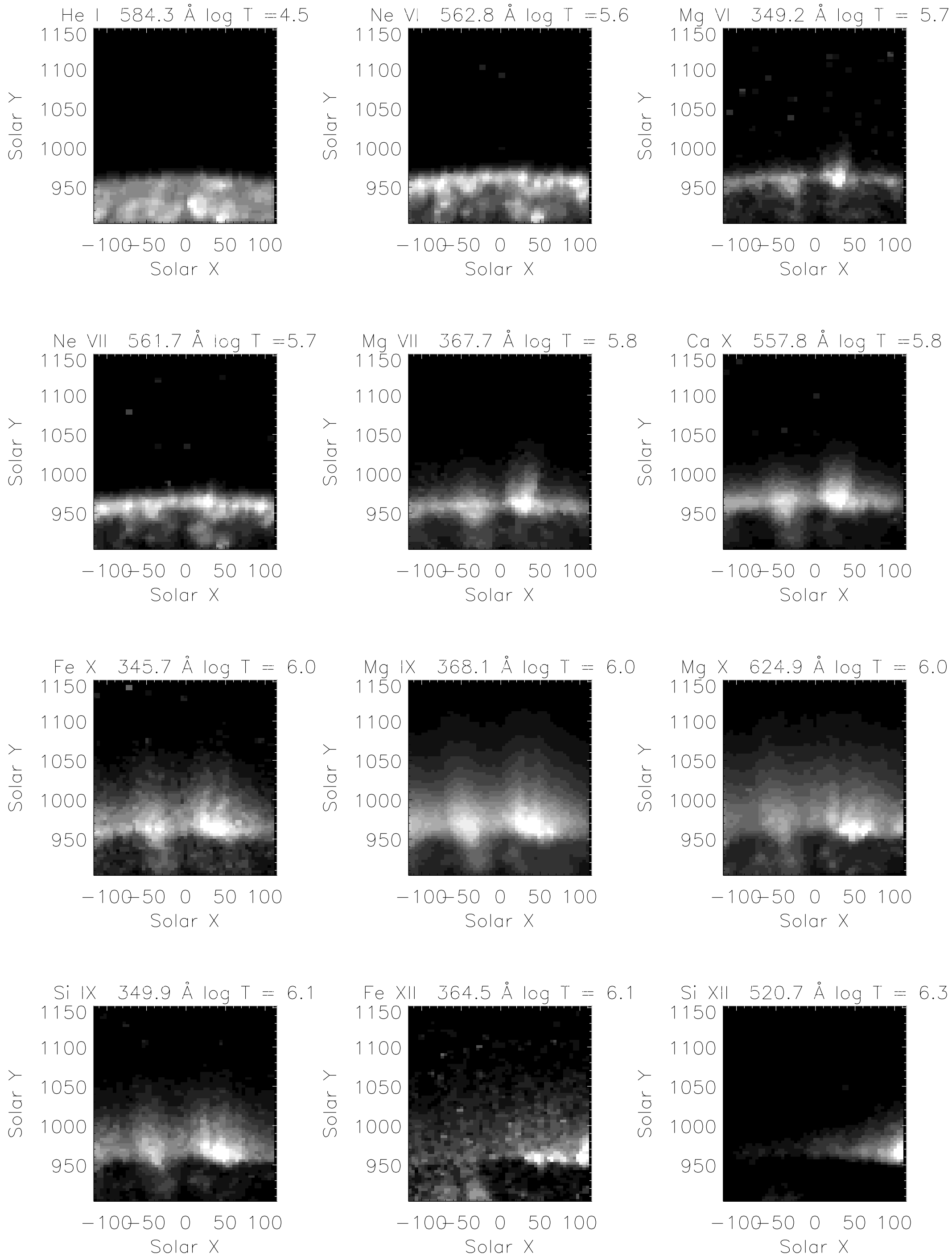

Figure 6.9: *Some off-limb monochromatic images from the CORO24W study – 12th October 1997.*

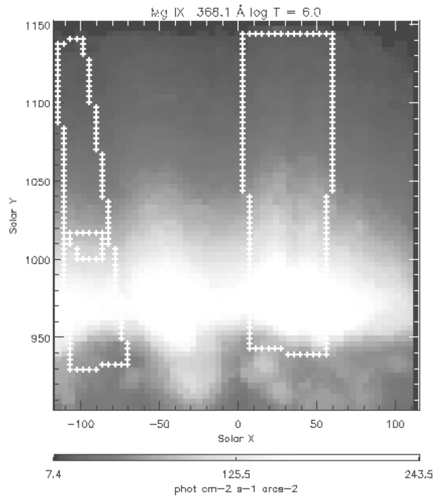

Figure 6.10: *Some selected areas – 12th October 1997. Left: a long, narrow inter-plume area for off-limb radial profiles, and a small area within it for a DEM analysis. Right: a plume area. The full-wavelengths $NISAT$ spectra were centred on the meridian, in the inter-plume region in the middle of the figure (see also Figure 4.9).*

In conclusion, the observations of 1997 October 12 illustrate the difficulties in dealing with off-limb coronal hole observations. Even with long exposures, the signal in coronal holes is low, and errors in the derivation of the parameters can be substantial. Contamination from background emission may be present (in this case in the form of diffuse background emission from hot plasma), even in regions that at first sight seem unaffected. This contamination probably affects all temperature estimates based on lines that are emitted at $T > 10^6$ K. The plasma distribution along the line of sight is not isothermal in most of the regions, except near the base of the plumes.

The off-limb observations of 1998 February 9

Other observations of plume and inter-plume regions off-limb were analysed, and showed a variety of results (that are not presented here), but which confirm that in general plumes are quasi-isothermal structures, having temperatures slightly lower than the surrounding coronal hole region. For example, a DEM analysis of an off-limb observation of the 9th February 1998 was performed over a plume region just $40''$off-limb and a nearby inter-plume region, at the same height from the limb. The plume showed an almost isothermal DEM distribution, with a peak temperature T = 8.1x10^5 K, while the adjacent region had a DEM with a peak at T = 8.5x10^5 K. In this observation the amount of quiet sun

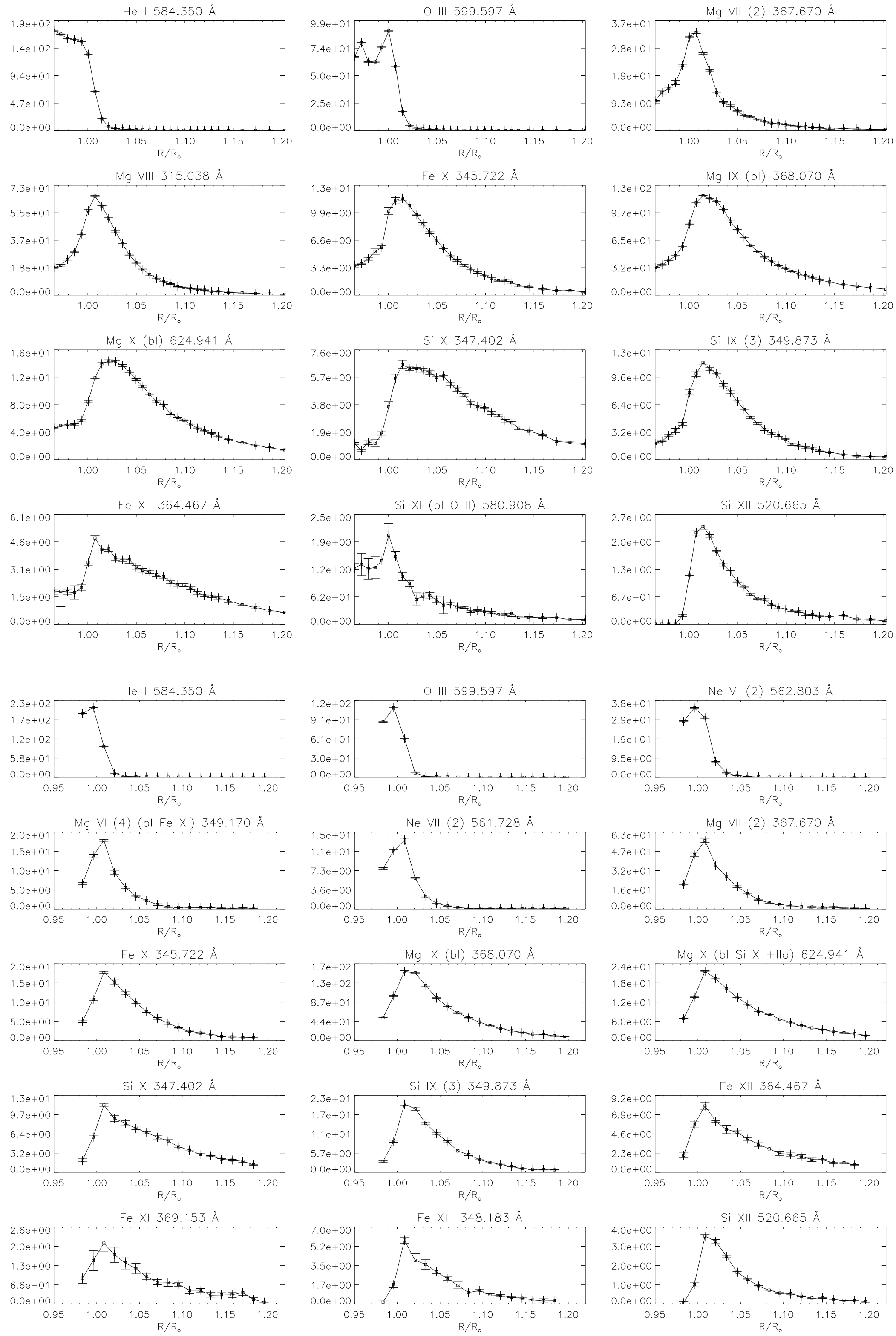

Figure 6.11: *The off-limb inter-plume (from NISAT_S5, upper 4 rows) and plume intensities (from CORO24W, below) – 12th October 1997.*

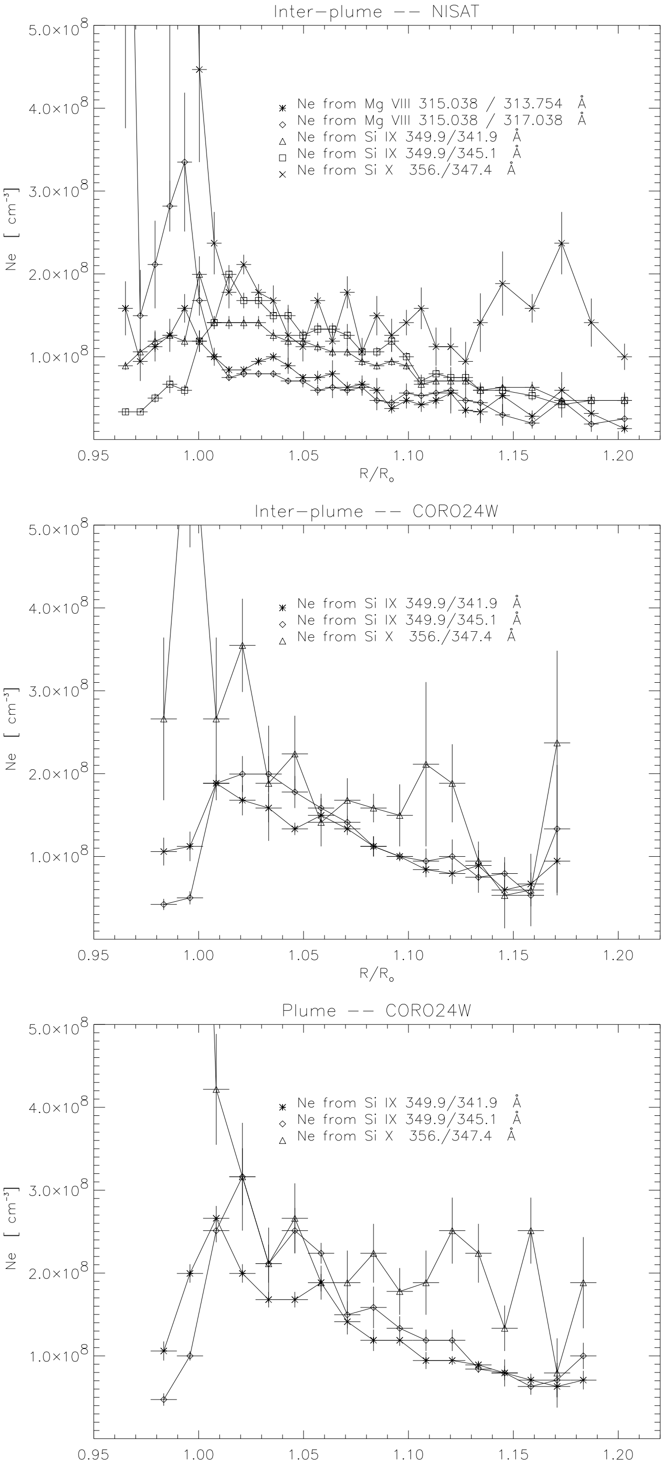

Figure 6.12: *The off-limb inter-plume (from NISAT_S5, top, and from CORO24W, middle) and plume (from CORO24W, bottom) densities – 12th October 1997.*

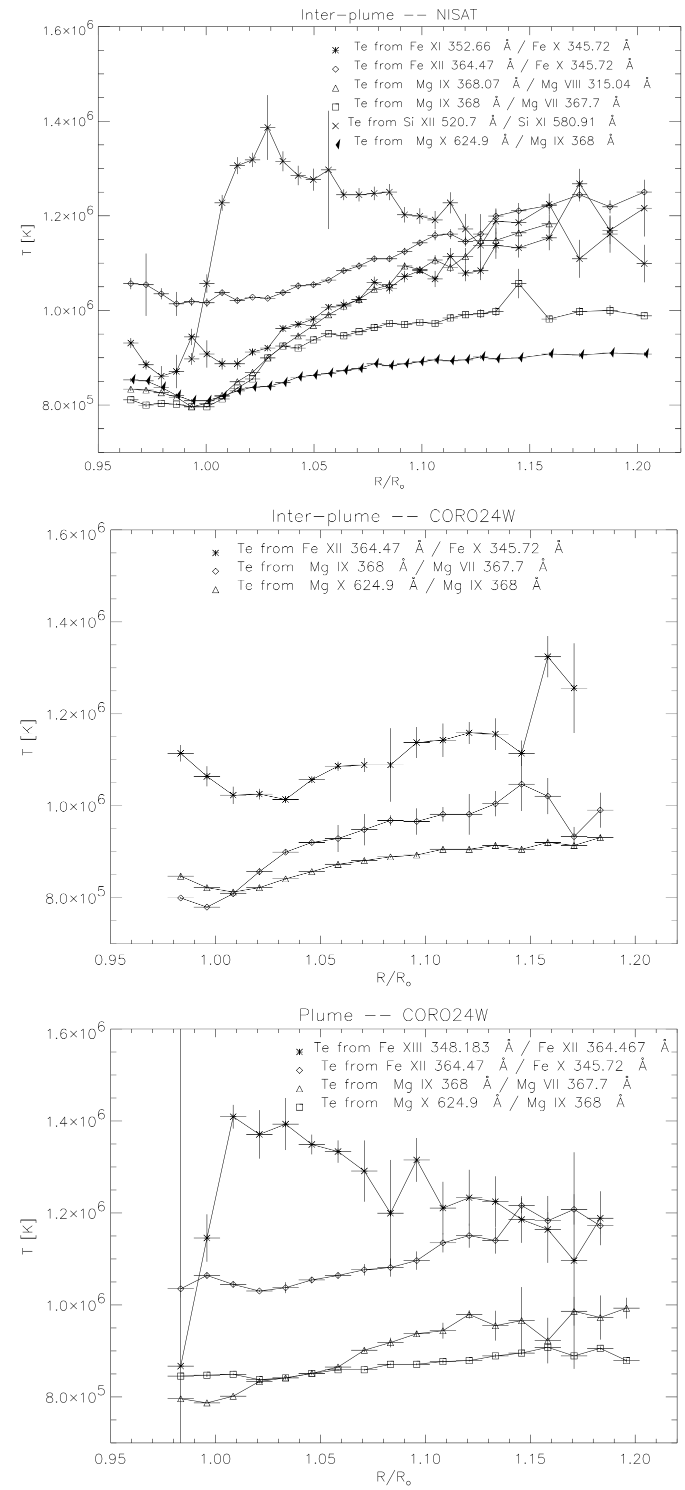

Figure 6.13: *The off-limb inter-plume (from NISAT_S5, top, and from CORO24W, middle) and plume (from CORO24W, bottom) temperatures, derived from various line ratios, assuming ionization equilibrium – 12th October 1997.*

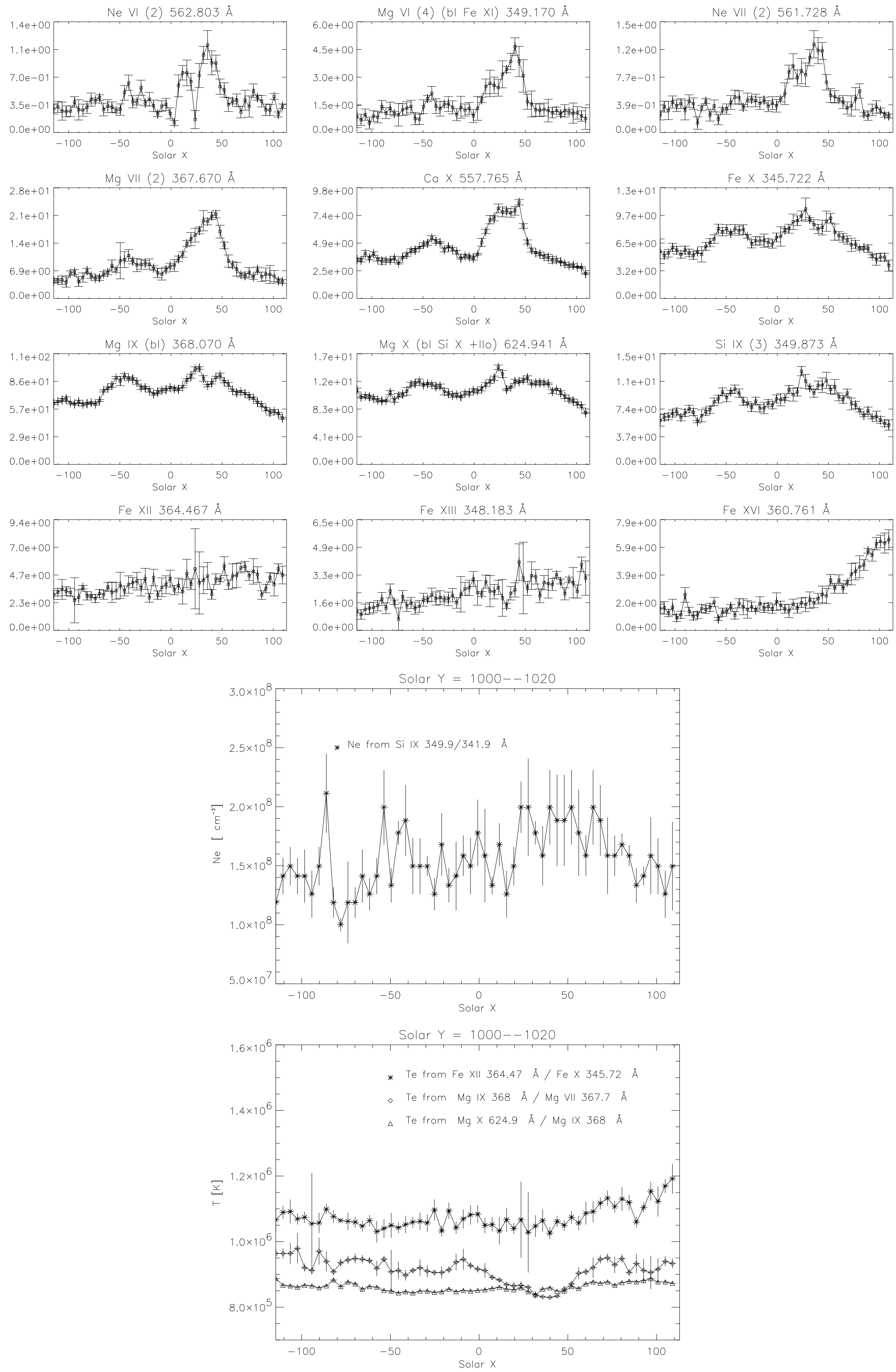

Figure 6.14: *Some intensity profiles across the plumes, at 1.05 $R_\odot$(above), with averaged densities and temperatures (below) – 12th October 1997.*

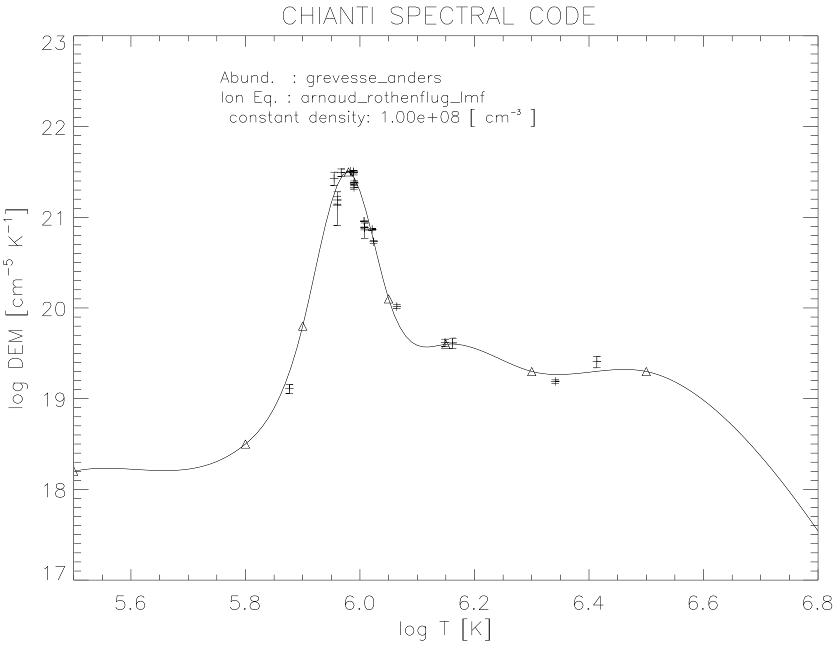

Figure 6.15: *The off-limb inter-plume DEM – 12th October 1997. Note the high-temperature tail, that is constrained up to log $T \sim$ 6.5 by the presence of high-temperature lines.*

material along the line of sight was low.

The GIS cross

Here some results from the off-limb GIS cross study of the 27th March 1997 are presented. The observations were performed over the south pole. The N-S scan observed a bright plume that was visible on the meridian (see Figure 4.10), from just inside the limb out to 1.1 $R_\odot$, while the off-limb E-W scan created a series of spectra across the plume, (Solar X = -60 : + 60), at a distance $\simeq$ 1.08 $R_\odot$. The plume lasted for the whole period of the GIS observation (almost 7 hours). The N-S scan was performed on the meridian (Solar X = 0), along the eastern edge of the plume.

Figure 6.16 shows the intensity profiles of some lines in the N-S off-limb observation, with averaged densities and temperatures derived from different line ratios. Note that the Fe X densities are in agreement with those derived from Mg VIII, off-limb, and that this plume had relatively high densities at the limb, and values $N_{\rm e} \simeq$ 1x10^8 cm^{-3} at 1.1 $R_\odot$. The temperatures derived from Fe ions are all consistent, showing this plume to be isothermal, and having slightly increasing temperatures ranging from $T \simeq$ 9x10^5 K near the limb, to $T \simeq$ 1.05x10^6 K at 1.1 $R_\odot$. This plume was therefore not only a very bright plume, but also a 'hot' one. A direct measurement of the electron temperature was attempted, using the Mg IX 368/706 Å ratio, but the values have a large scatter, due to the low signal and the fact that the Mg IX 368 Å was strongly ghosting. No conclusive results could be obtained.

Figure 6.17 shows the intensity profiles of some lines in the E-W observation, with densities and temperatures as derived from different line ratios. Note how the plume is still visible at that distance, in all the lines (except at high-temperature), and is centred around Solar X = $20''$, about $40''$wide. The densities derived from Mg VIII do not show appreciable variation across the plume, while those derived from Fe X show an increase. Interestingly, the temperatures derived from the Fe ions only show a very small decrease in the temperature, where the plume was, showing that at that distance the plume was isothermal with the inter-plume region (with $T \simeq 1.03\text{x}10^6$ K).

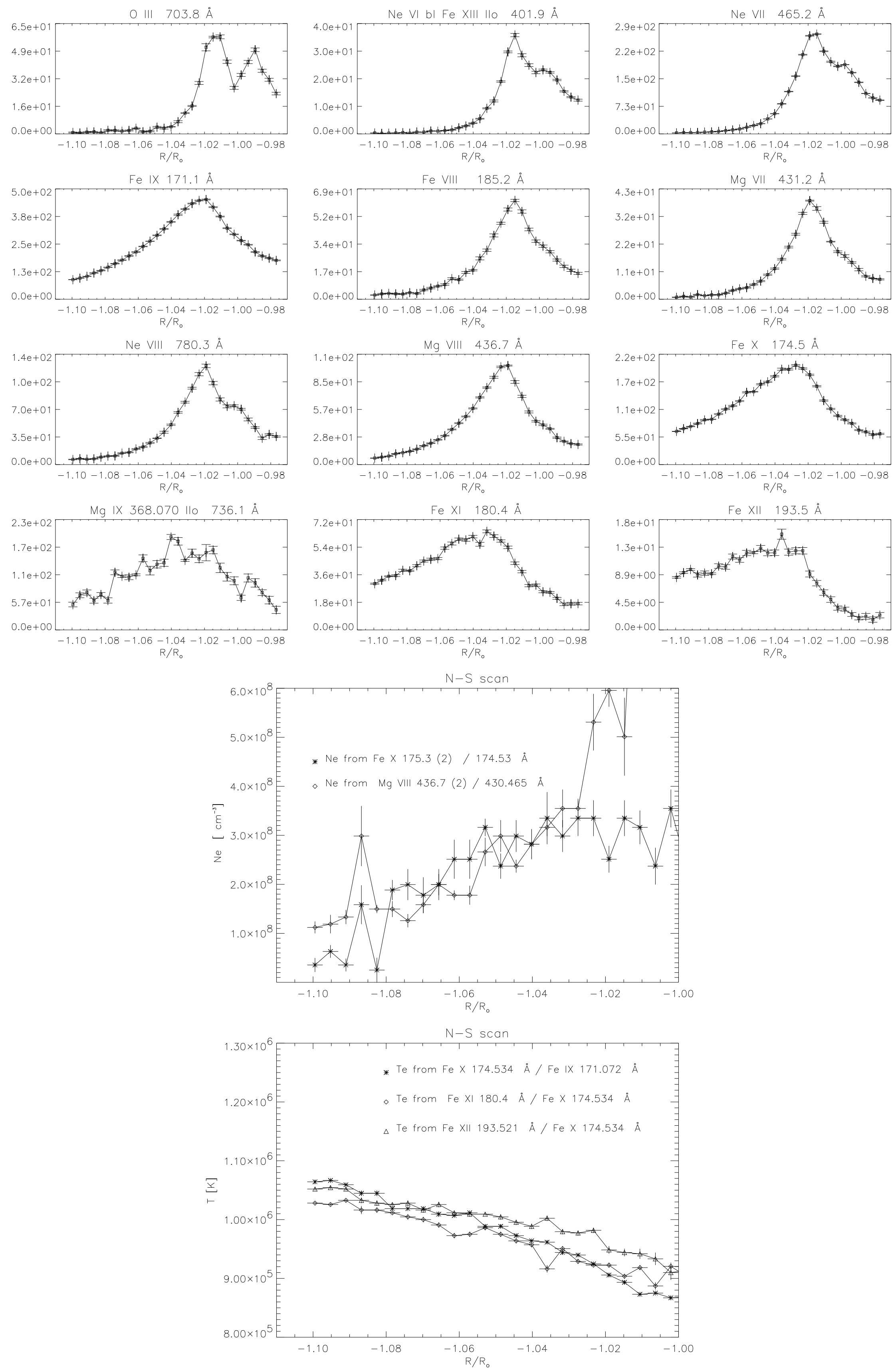

Figure 6.16: *The GIS N-S off-limb scan along a plume – 27th March 1997. Some intensity profiles (above), averaged densities and temperatures derived from different line ratios (below).*

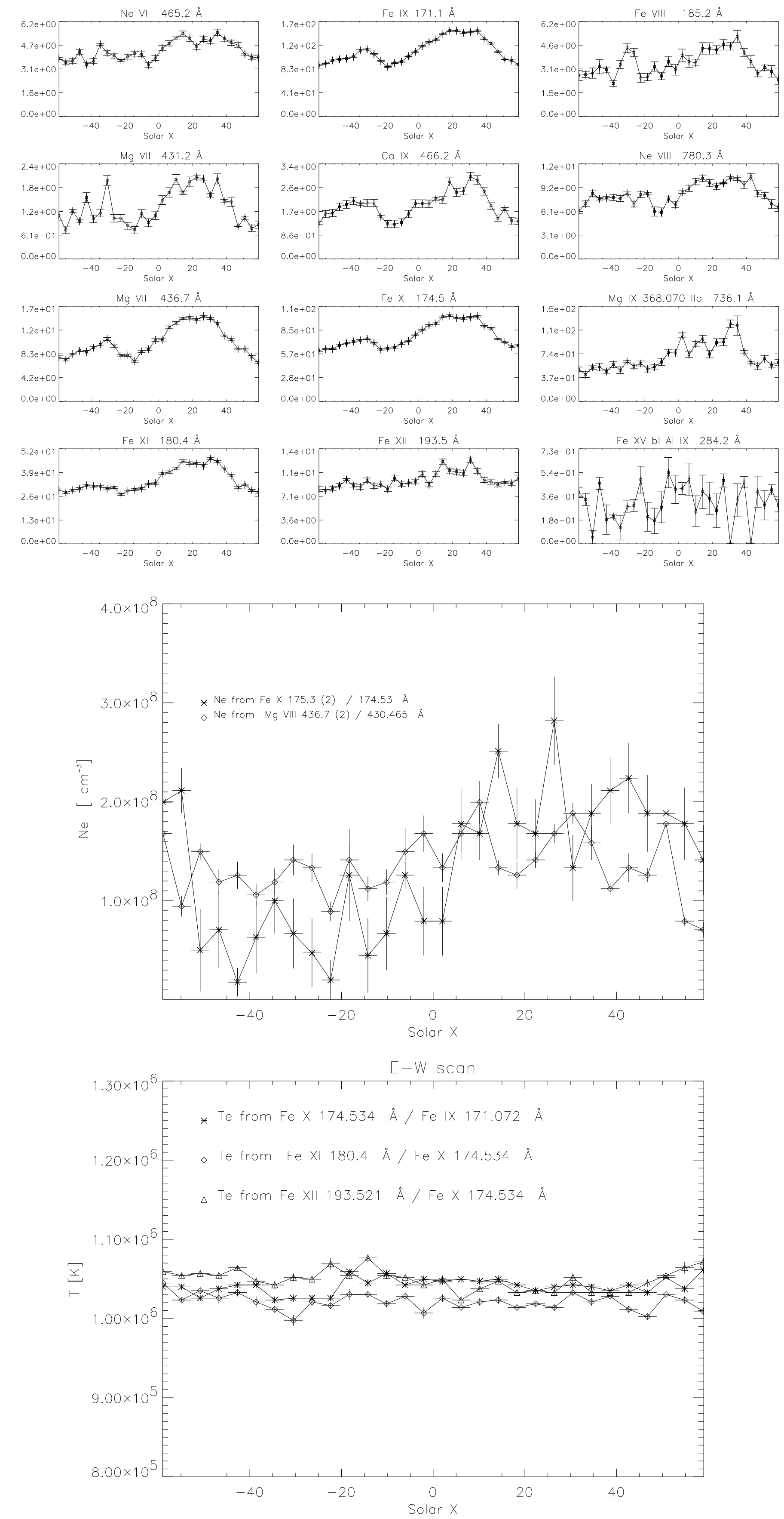

Figure 6.17: *The GIS E-W off-limb scan across a plume, at $R \simeq 1.08\ R_\odot$– 27th March 1997. Some intensity profiles (above), averaged densities and temperatures derived from different line ratios (below).*

6.3 Polar plumes observed on-disc

Observations of two polar plumes seen on the disc are presented here and compared to nearby coronal hole regions and to the observations of the low-latitude plume described in Chapter 5. The two polar plumes were seen on the 23rd August 1996 and on the 11th of October 1997. These plumes were stable structures lasting for several days in the north polar coronal hole. A Joint Operation Programme (JOP # 42) was organised by C. Deforest to observe the first plume. During this programme, all SOHO instruments carried simultaneous observations. The CDS observations have been planned, executed and analysed by the author. The analysis of a time sequence of CDS large-field-of-view observations of this plume has shown that this feature was stable during the whole observing period (few hours). The second plume, is the one already mentioned and observed on October 10 1997.

The two plumes discussed here are considered to be typical faint plumes as observed by CDS during the minimum of the solar cycle. They were found to have the same main characteristics as the equatorial plume (i.e. lower temperature, increased Mg/Ne and O/Ne intensities, visibility in only a few lines emitted over a limited temperature range) thus confirming the identification of the low-latitude feature as a plume. However, an analysis of CDS observations of many plumes has revealed that some do show different characteristics, for example some plumes had compact EUV enhancements at their base, and were very hot and dense (see *Bromage et al.*, 1997b, and *Young*, 1999).

Plumes seen on the disc were chosen, because in this case it is possible to distinguish them from the coronal hole regions and see their base. In coronal hole off-limb observations, it is in fact more difficult to exclude the possibility that there might be some plume material (from plumes rooted on the far side of the Sun) contaminating the 'true' coronal hole regions, thus affecting measurements of densities and temperatures. In addition, there might be more than one plume along the line of sight.

The principal aims of the rest of this Chapter are: to describe how plumes can be recognised from their appearance in CDS spectra; to apply spectroscopic diagnostic techniques to CDS observations in order to characterise plumes in terms of densities, temperatures and element abundances; to point to the complexity of the interpretation of such data, in particular when element abundances are deduced; and to clarify some observational points, in particular showing how plumes appear in EIT images. No attempt is made to study the evolution of plumes, where imaging instruments such as EIT are more appropriate.

In the EUV, plumes are known to be visible only in emission lines that form over a narrow range of temperatures (e.g., *Widing and Feldman*, 1992), with emission almost absent from ions that form at temperatures above a million degree. It has been therefore quite surprising to see plumes with the SOHO EIT 195 Å filter, where the emission is generally assumed to be due to Fe XII, which has an ionization equilibrium temperature $T_e \simeq 1.6 \cdot 10^6$. Nevertheless, *DeForest et al.* (1997) use EIT 195 Å and 171 Å images to estimate plume temperatures. In order to check the validity of this broad-band filter ratio estimate, a comparison between EIT and CDS observations of one polar plume is presented in Section 6.3.3 below.

6.3.1 Results for a polar plume observed on 1996 August 23

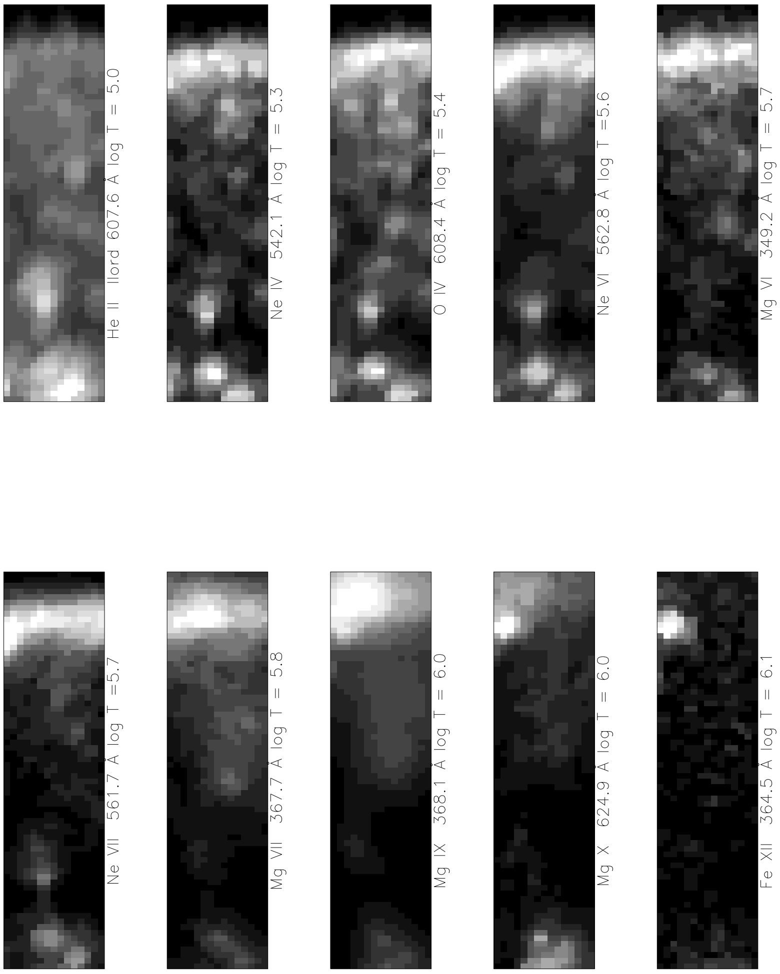

Figure 6.18: *Monochromatic images of the NIS observation – 23rd August 1996. The plume is seen best in Mg VII and Mg IX, with its base near the centre of the raster and the 'plume' extending up to the limb (and above).*

Fig. 6.18 shows monochromatic images of the region rastered by the NIS on 1996 August 23. This plume presents the typical characteristics of plumes as observed by CDS. The peak of the emission in the plume is in the upper transition region lines Mg VII, and Mg IX. The plume is not visible in the high-FIP Ne lines, nor in the high-temperature (e.g. Fe XII) lines. The cooler lines (He II,Ne IV) show the cell centre - network pattern.

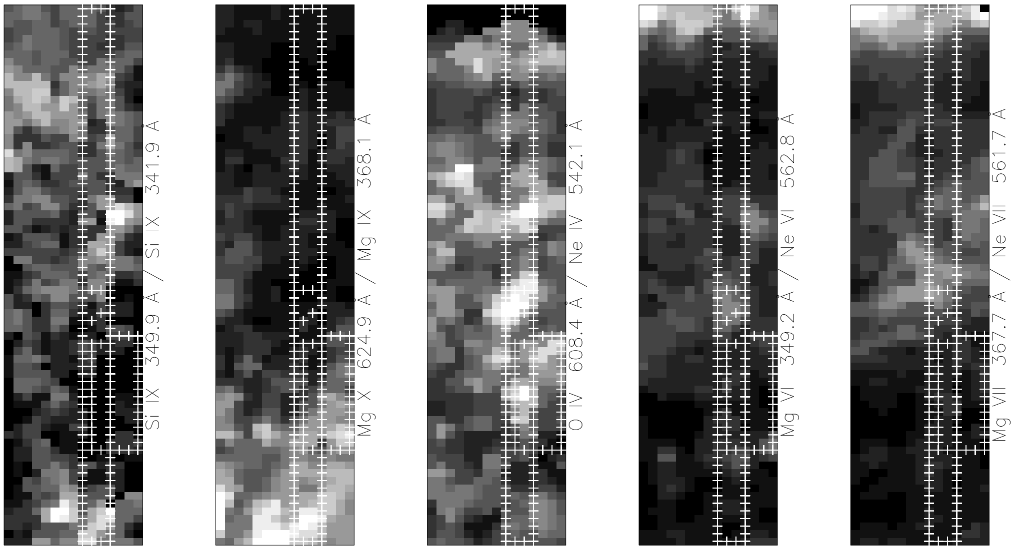

Figure 6.19: *Ratio images of the NIS observation – 23rd August 1996, showing density ratios (Si IX); temperature ratio (Mg X / Mg IX); and O/Ne, Mg/Ne line ratios, indicating relative abundances. Selected areas are over-plotted. The plume area is a small region (within the long thin area) indicated by four '+' characters.*

Since the plume was aligned at an angle to the line of sight, the peak of the emission appears at different spatial locations, when lines emitted at different temperatures are examined. Strictly speaking, only the emission of lines of similar temperatures comes from the same region along the line of sight.

Intensity ratios of lines can give some indications of variations of density, temperature and abundances across the plume. Figure 6.19 shows some intensity ratio images, which indicate that the plume area has lower temperature, and at the base has increased Mg/Ne and O/Ne intensities (with values similar to those of the low-latitude plume, discussed in Chapter 5.

In order to increase the S/N, averaged spectra of three regions, shown in Figure 6.19, have been extracted: a profile along the plume, in the N-S direction; a region at the base of the

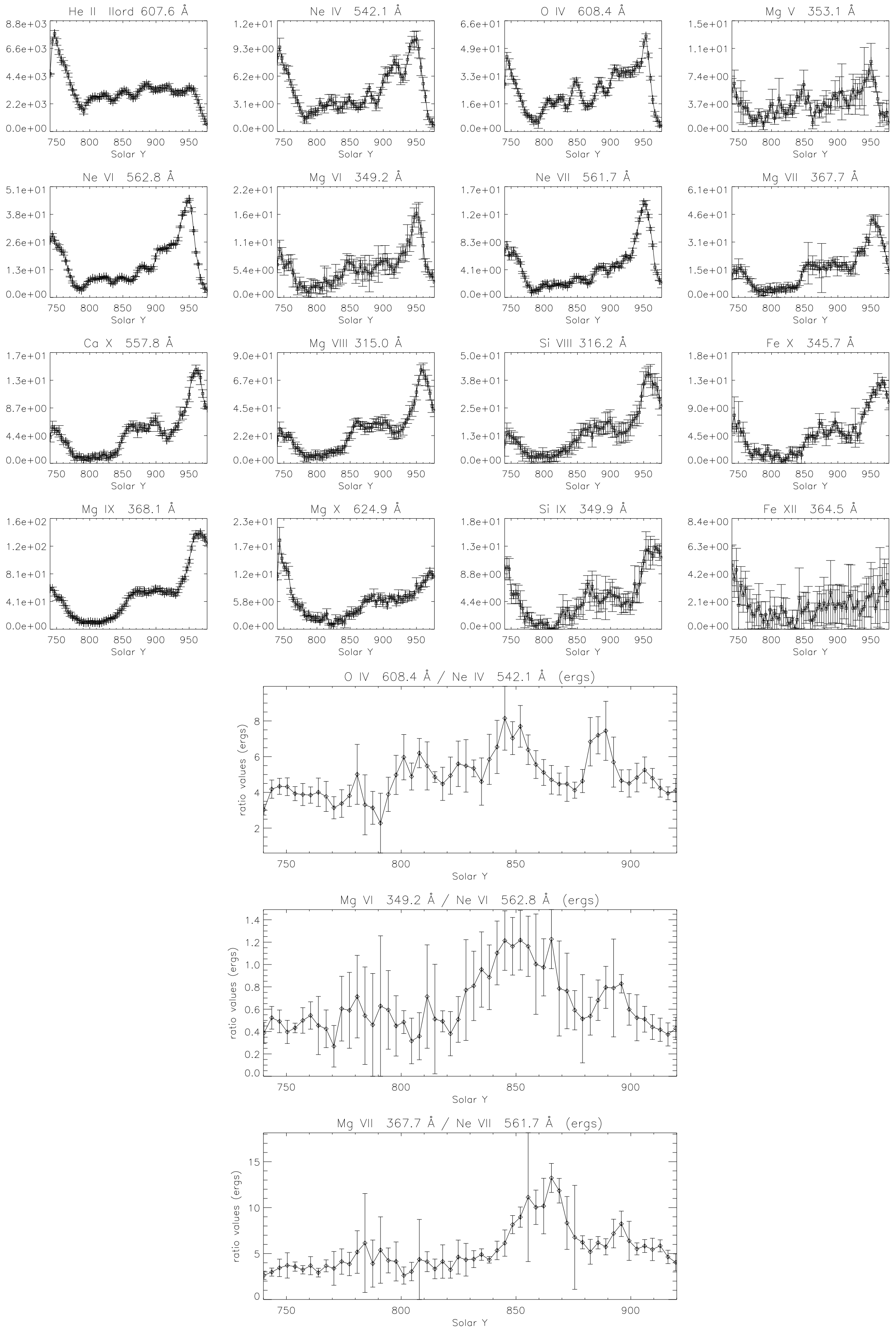

Figure 6.20: *Intensities of a selection of NIS lines along the N-S direction, with corresponding intensity ratios – 23rd August 1996.*

plume; and a coronal hole region to the SW of the plume.

Figure 6.20 shows the profiles of the intensities and the ratio of intensities of some selected lines from the N-S scan, from which it appears clear that the base of the plume (situated around Solar Y=850) is close to a network junction (where SOHO/MDI magnetograms show a concentration of unipolar flux). Note that lines emitted at higher temperatures have a peak emission shifted toward the North, due to the tilt effect, so it is difficult to locate the base of the plume precisely relative to the network revealed in cooler lines.

The O/Ne and Mg/Ne ratios clearly show the presence of the plume base at Solar Y=850, and also indicate a possible second plume in the line of sight at Solar Y=890. These ratios also indicate that it is probably the Ne abundance that is varying. Indeed, a preliminary DEM analysis of this plume region has confirmed that the Ne/O abundance has a value lower than photospheric, by a 0.2 dex.

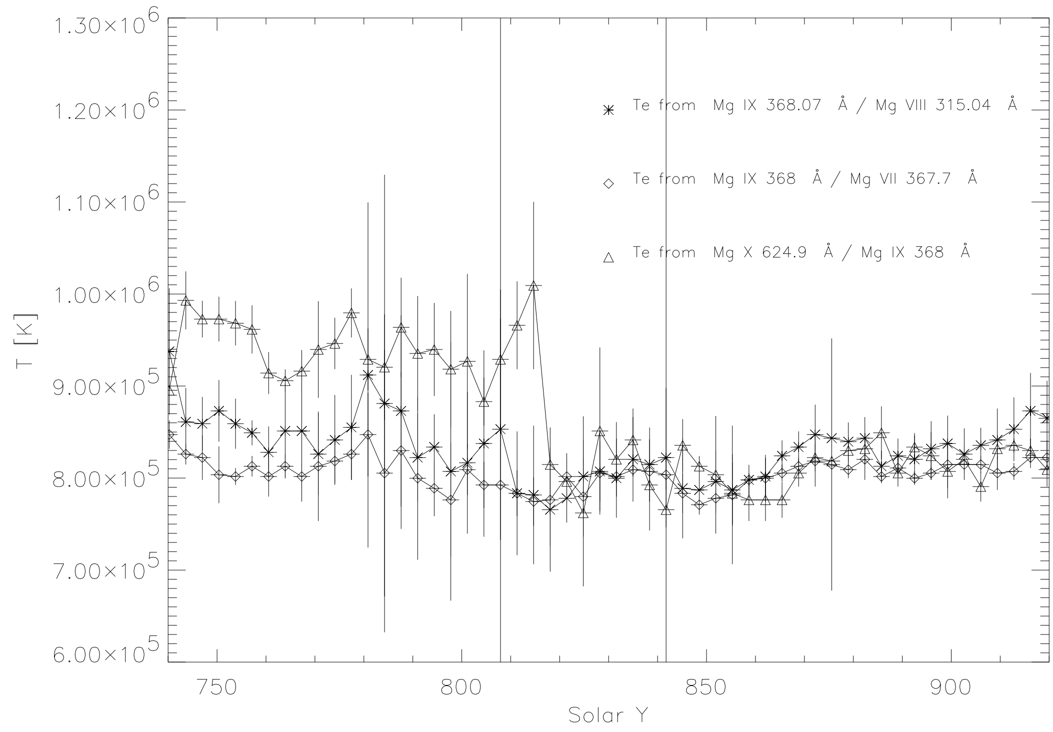

Figure 6.21: *Isothermal temperatures along the N-S scan – 23rd August 1996. Note that the plume lies along this scan, above about 825 ″(solar Y). This is the region where the temperature profiles become coincident, indicating isothermal plasma.*

Figure 6.21 shows isothermal temperatures derived from different ratios. Note that the three different line ratios produce different temperatures in the coronal hole region, while in the plume region they are in close agreement, another strong indication of plumes being quasi-isothermal.

Table 6.2: Table of parameters deduced from the 23rd August 1996 averaged spectra of the selected regions.

	plume base	Coronal hole
N_e (O IV 625.8/608.4 Å)	7.5±4 10^9	7.1±1 10^9
N_e (Mg VIII 315.0/317.0 Å)	1.2±0.8 10^8	0.6±0.4 10^8
N_e (Mg VIII 315.0/313.7 Å)	0.8±0.5 10^8	0.7±0.4 10^8
N_e (Si IX 349.9/341.9 Å)	1.3±0.8 10^8	0.5±0.5 10^8
N_e (Si IX 349.9/345.1 Å)	0.9±0.8 10^8	0.2±0.2 10^8
T_e (Mg X 624.9 Å/ Mg IX 368 Å)	8.1±0.2 10^5	8.9±0.2 10^5
T_e (Mg IX 368 Å/ Mg VIII 315.0 Å)	8.0±0.1 10^5	8.2±0.3 10^5
T_e (Mg IX 368 Å/ Mg VII 367.7 Å)	7.8±0.1 10^5	7.9±0.8 10^5
I([O IV 608.4 Å/ Ne IV 542.1 Å])	7.4±0.9	4.5±0.2
I([Mg VI 349.17 Å/ Ne VI 562.8 Å])	1.1±0.1	0.4±0.1
I([Mg VII 367.67 Å/ Ne VII 561.7 Å])	7.1±1	4.1±3

Table 6.2 shows the values of the parameters deduced from the averaged spectra of the plume base and the nearby coronal hole region. Although the results have relatively large errors, the indication is that the density in the plume area was $N_e \simeq 1\text{x}10^8$ cm^{-3}, about a factor of two higher than the nearby coronal hole region, which had a very low density. The temperature ratios indicate a more isothermal distribution inside the plume ($T \simeq 8\text{x}10^5$ K), with lower temperatures than in the coronal hole area.

6.3.2 Results for a polar plume observed on 1997 October 11

The second plume was also a long-lasting structure that was visible during the second week of October 1997 in the north polar hole. Fig. 6.22 displays a sequence of EIT 171 Å images, showing the stability of this plume over a period of a few days. A series of CDS observations of this plume were performed, of which only those of the 11th of October 1997 are presented here. On this day, CDS was in high-telemetry mode, i.e. the information was telemetered to the ground at double the normal rate.

The NIS observations presented here used the UCLAN_N3 study. The UCLAN_N3 covered a large area (2'x3', see Fig. 6.23) in about 40m (with a 60s exposure time, high-telemetry) starting at 15:00:37 UT.

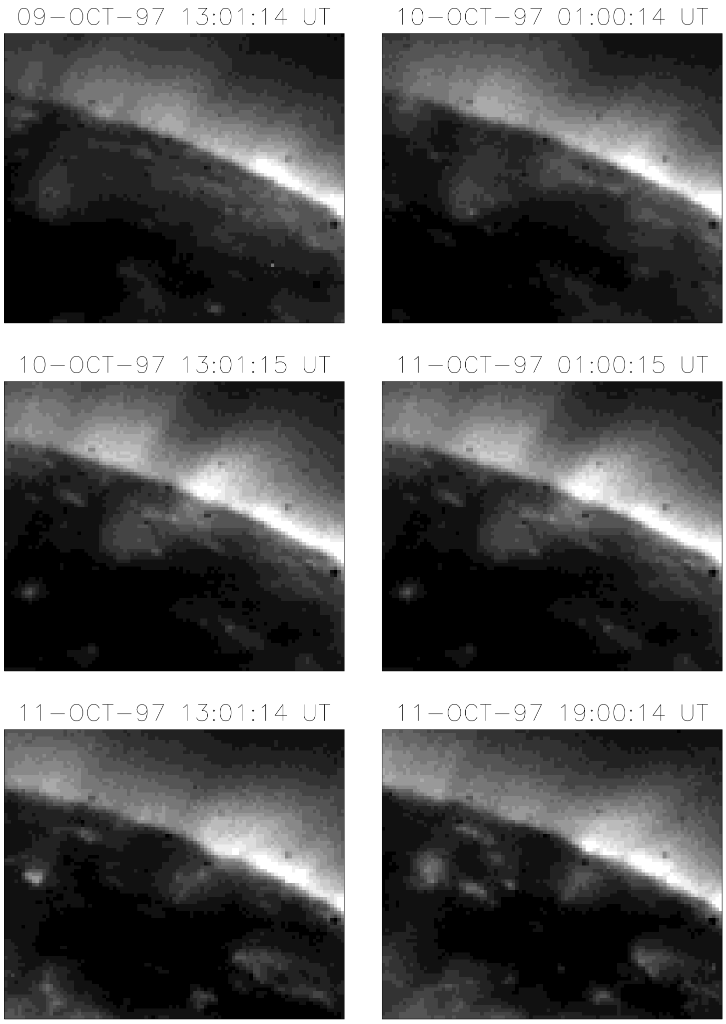

Figure 6.22: *Sequence of SOHO EIT 171 Å images of the north polar coronal hole, showing the persistence of a polar plume.*

Figure 6.23 shows monochromatic images of the region rastered by the NIS. This plume shows the same characteristics as the plume of the 23rd of August 1996, i.e. maximum visibility in the upper transition region lines Mg VI, Mg VII, Ca X, Mg VIII, Mg IX, and it is not visible in the high-FIP Ne lines, nor in the high-temperature lines. The intensities of the He II, and Ne V lines show the presence of a network boundary close to the base of the plume. This plume is also tilted, compared to the line of sight, and the comparison between lines that are formed at very different temperatures should be made with caution, as in the previous case.

The ratio images in Figure 6.24 show a marked decrease of the temperature and increase of Mg/Ne and O/Ne intensity ratios at the base of the plume, again indicating a decrease in the Ne abundance.

A GIS scan across the plume, starting at 16:16:40 UT was performed after the NIS observation. This GIS observation used the high-telemetry *study* HRBNDWE, where the $4''$x $4''$slit is rastered from west to east in order to cover a $4''$x $60''$region with 15 spatial positions. For each of these positions, GIS recorded 100 exposures of 5s each, in a time span of 11m. It took about 2h50m to scan the whole $4''$x $60''$area. The GIS observed the plume region about one hour after NIS observed it. In order to increase the S/N, the data analysis on the GIS spectra was performed on the average of the 100 exposures, one for each spatial location (although a preliminary study of the high time variability was performed).

The intensities of the NIS lines have been extracted from NIS spatially-averaged spectra over the region rastered by the GIS. The NIS and GIS observations were not simultaneous, and an instrument repointing took place between the two observations. The analysis of the NIS and GIS observations has shown a need to adjust the position of the GIS rasters by $10''$, relative to the position of the NIS observations. With this small adjustment, most of the lines have similar profiles across the plume, as shown in Figure 6.25 (and in particular this is true for the few lines that are visible in both GIS and NIS). Only the low-temperature lines present some differences, as expected. Nevertheless, in both GIS and NIS lines it is evident that the base of the plume is near a network region (i.e. a region where the low-transition region lines are enhanced).

Figure 6.25 shows how the intensities of several GIS and NIS lines vary across the plume. The upper transition region lines increase by a factor of about 4 in the plume area, while the high-temperature lines do not show any increase in intensity.

Figure 6.26 shows isothermal temperatures and densities across the plume. There are indications of a density increase inside the plume area, but they are within the errors. What is more obvious is a more isothermal temperature and a sharp decrease in the value

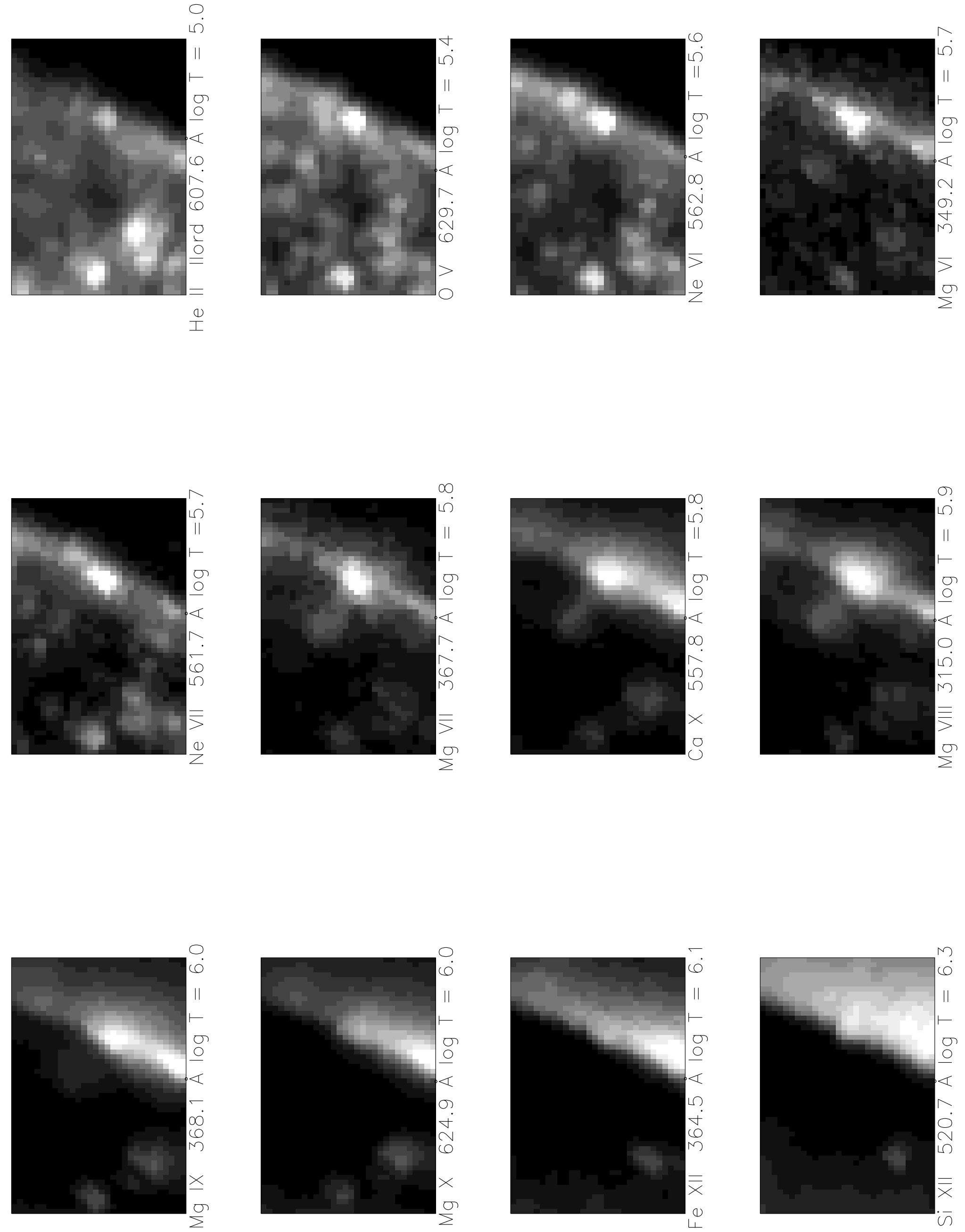

Figure 6.23: *Monochromatic images of the NIS observation – 11th October 1997.*

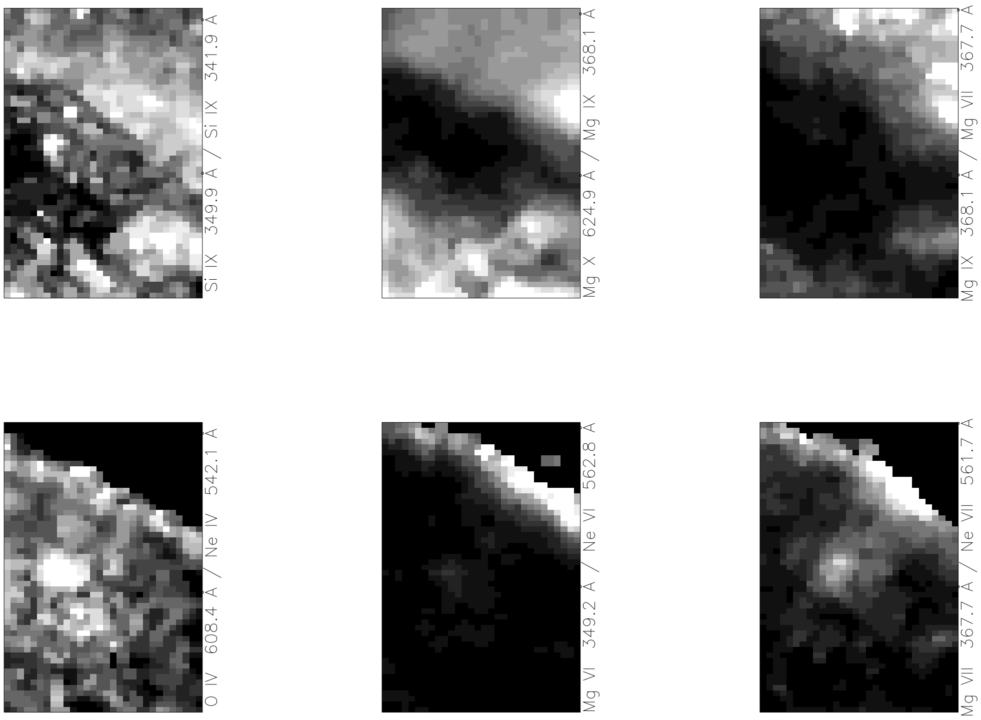

Figure 6.24: *Ratio images of the NIS observation – 11th October 1997. A density ratio (Si IX), a temperature ratio (Mg X / Mg IX) and abundance ratios (O/Ne and Mg/Ne) are shown. Note the high O IV/Ne IV and Mg/Ne intensity ratios at the base of the plume.*

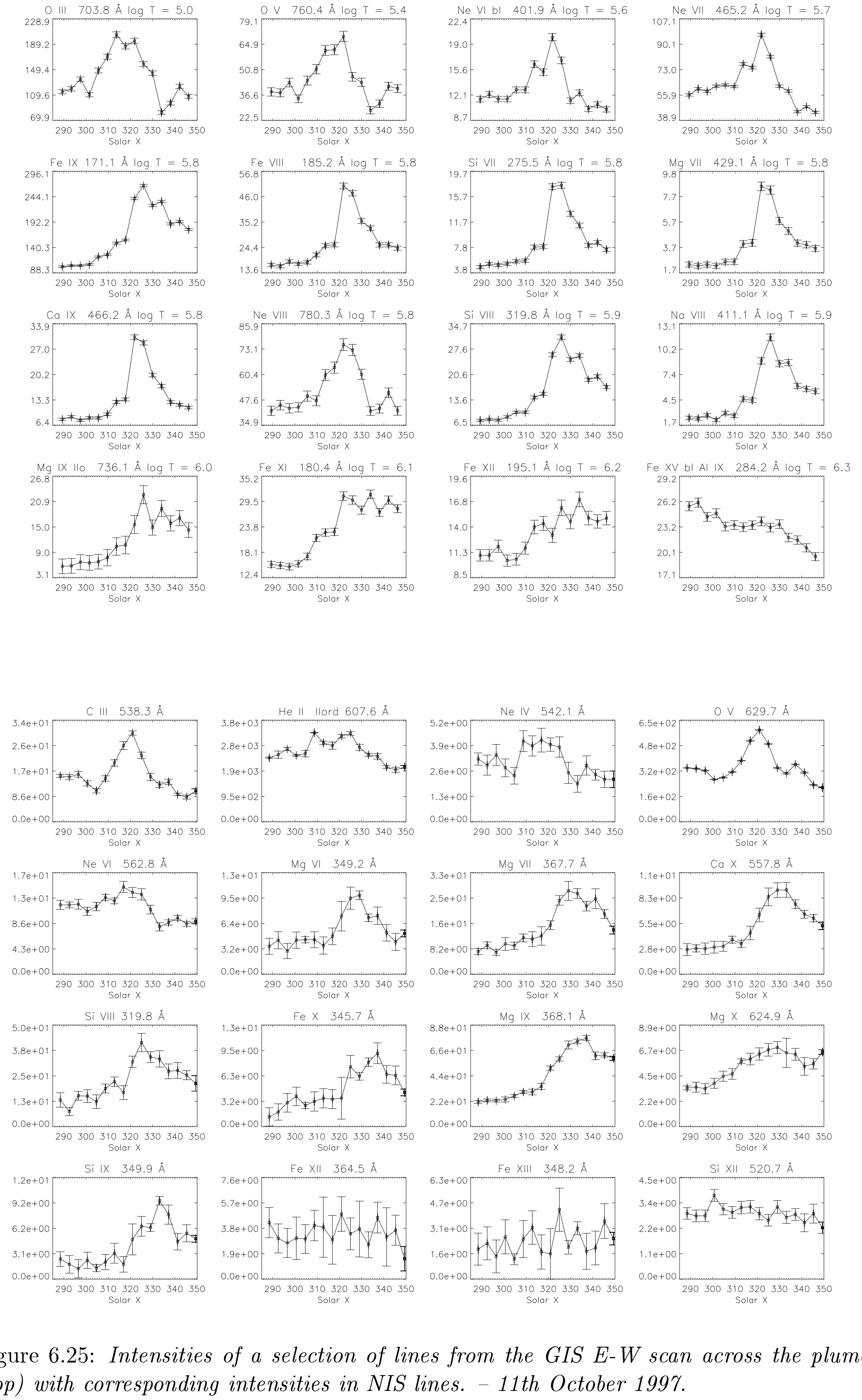

Figure 6.25: *Intensities of a selection of lines from the GIS E-W scan across the plume (top) with corresponding intensities in NIS lines. – 11th October 1997.*

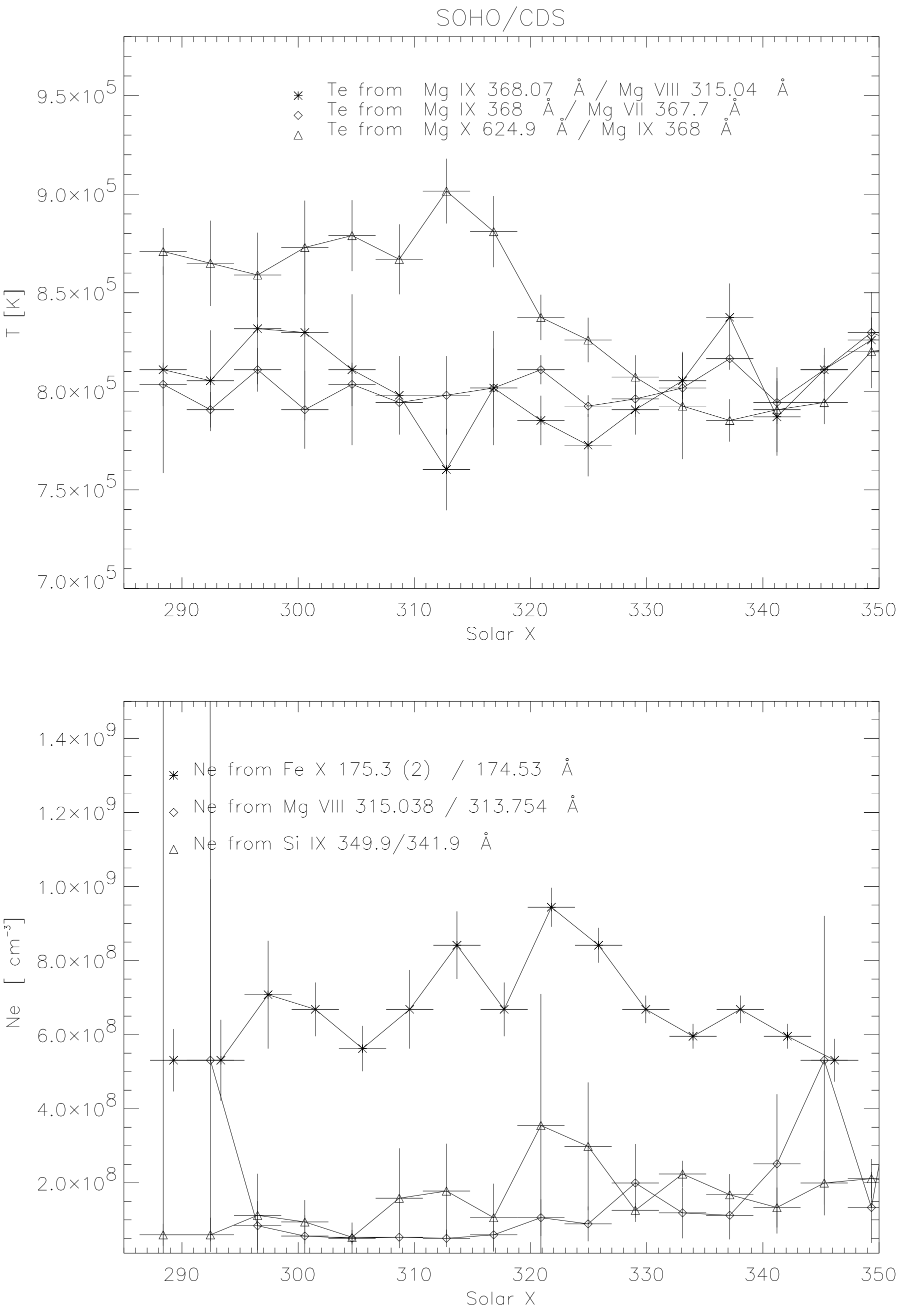

Figure 6.26: *Isothermal temperatures and densities across the plume – 11th October 1997.*

derived from Mg X / Mg IX, (as already seen for other plumes).

Figure 6.27 shows some intensity ratios derived from the GIS and NIS observations. All the low-FIP to high-FIP intensity ratios undoubtedly show a large increase in the plume, and therefore a probable FIP effect, while the O/Ne ratios also show variations, as was observed for the plume of the 23rd of August 1996 and the equatorial plume.

Other ratios examined (e.g. Mg/Si) indicate that the relative abundances between the low-FIP elements remain almost unchanged.

Two spatial positions have been selected as representative of the coronal hole and plume areas, at $SolarX = 289$ and 326, respectively. For these areas, the intensities of the GIS and NIS lines have been considered jointly, in order to characterise the plasma. This might not be valid, because of the lack of co-temporality between the GIS and NIS observations, but is justified by the stability of the plume and the similarity between the observations of common lines. Considering NIS and GIS line intensities at the same time has great advantages. The cross-calibration studies performed on the 1st and the 16th of October (outlined in Chapter 3) produced confidence in the stability of the CDS detectors, and on the reliability of using GIS and NIS together. Only a 30% correction factor was applied to all the calibrated GIS lines, for the plume region, possibly indicating that the field of view was slightly different between the two observations. The source region in each case is only $4''$x$4''$, while the width of the plume is typically $20''$, so although it is clear that both NIS and GIS observations are within the plume, the lower signal may indicate that this source is nearer the edge.

Figure 6.28 shows a comparison between the GIS spectra of the coronal hole and plume areas. There are large differences in the intensity of upper transition region lines (e.g. Mg VI, Mg VII, Mg VIII), together with a small decrease of the high-temperature lines (e.g. Fe XV) in the plume data, and a variation of the Mg/Ne and Ca/Ne ratios, as already discussed. In particular the region around 402 Å shows how different the spectra are. Other parts of the GIS spectra are shown in Figs. 6.31 and 6.32 (see Section 6.3.3, where the GIS-EIT comparison is presented), and also stress the different temperature structure between the coronal hole and the plume area examined. Lower temperature lines (such as Fe VIII) increase their intensity inside the plume. The complete GIS spectra are also shown in Figures E.1, E.2, E.3, E.4.

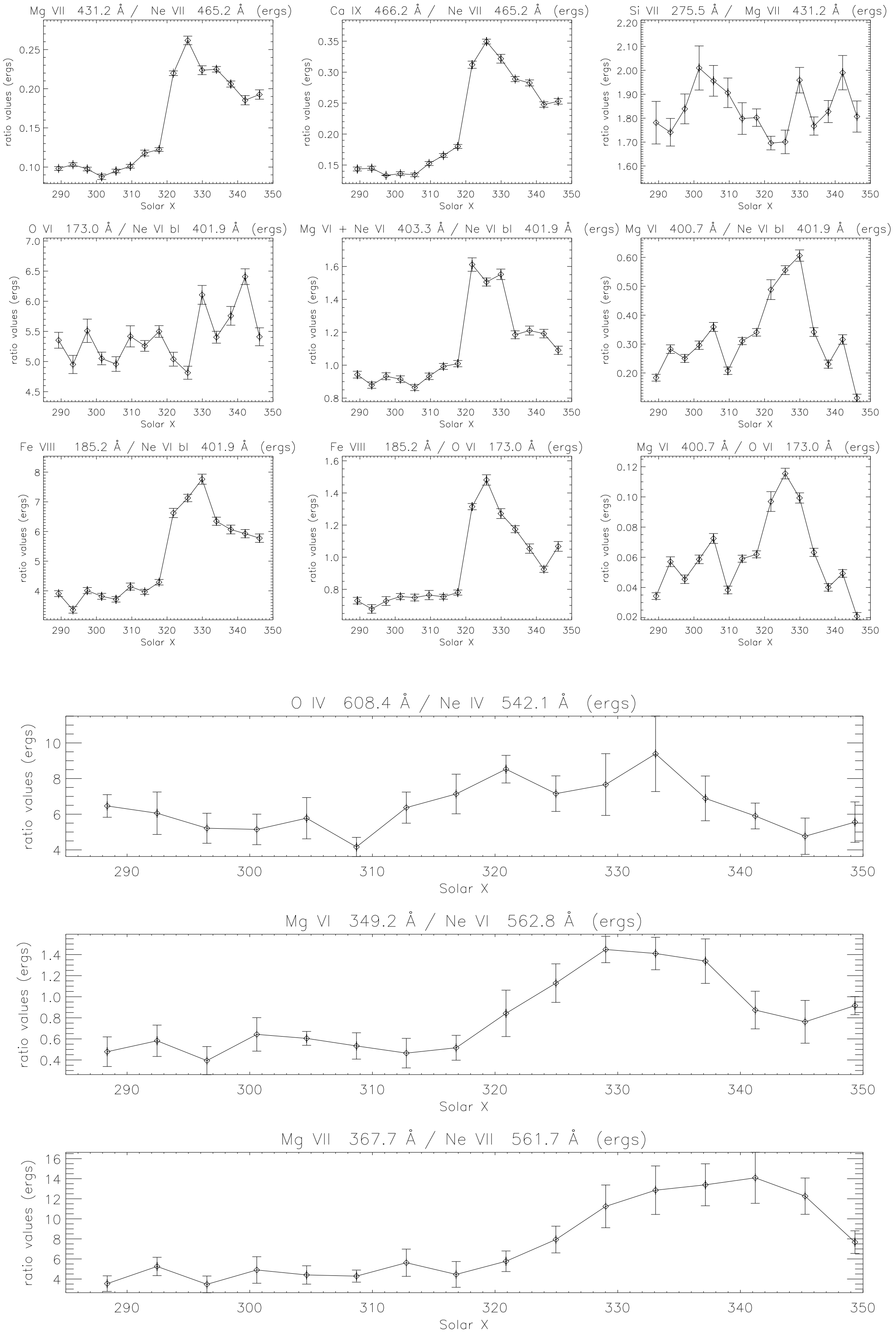

Figure 6.27: *Intensity ratios of selected lines of the GIS E-W scan across the plume (top) with corresponding ratios of NIS lines – 11th October 1997.*

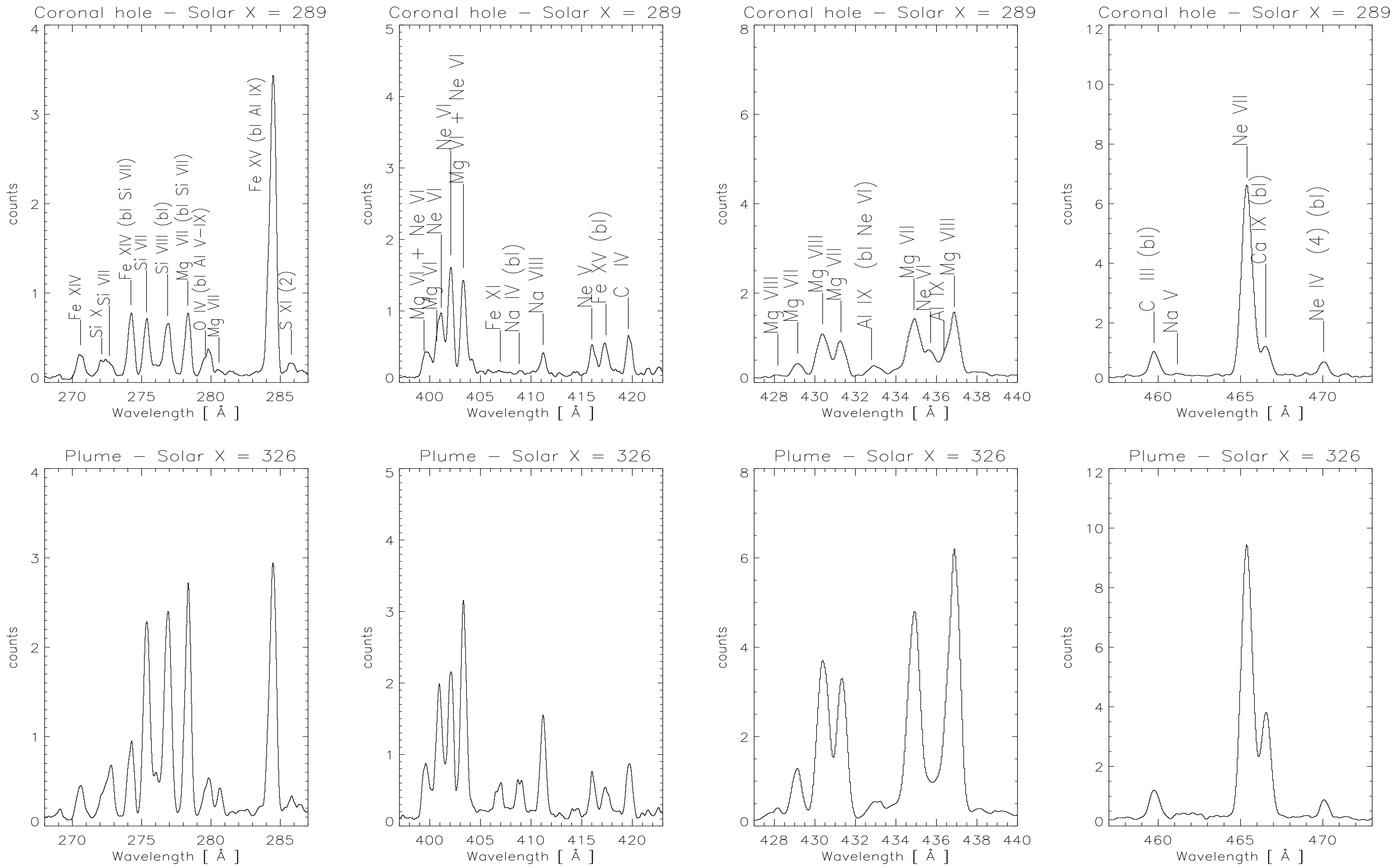

Figure 6.28: *GIS spectra in selected wavelength regions, for the coronal hole (above) and plume (below) areas – 11th October 1997.*

Table 6.3: *Table of parameters deduced from the 1997 October 11 CDS spectrum of the base of a plume. The densities are in cm^{-3}, while temperatures are in K. Some intensity ratios, indicative of elemental abundance differences, are also shown. The element abundances, deduced from the DEM analysis, are shown at the bottom as logarithmic differences relative to the photospheric values (*Grevesse and Anders*, 1991), i.e. they are quoted in dex in the standard way. The elements are ordered by their FIP value, indicated in parentheses.*

N_e (O IV 625.8/608.4 Å)	5±3 10^9
N_e (Mg VII 319.0 / 367.7 Å)	3.8±2 10^9
N_e (Si IX 349.9/341.9 Å)	3.±2 10^8
N_e (Si IX 349.9/345.1 Å)	1.2±0.7 10^8
N_e (Mg VIII 315.0/317.0 Å)	0.8±0.7 10^8
N_e (Mg VIII 315.0/313.7 Å)	0.9±0.7 10^8
N_e (Fe X 175.3 (2) / 174.53Å)	8.5±0.6 10^8
N_e (436.7 (2) / 430.465 Å)	2.2±0.7 10^8
N_e (Fe XIII 203.8 (2) / 202.0 Å)	1.8±0.5 10^8
T_e (Mg X 624.9 Å/ Mg IX 368 Å)	8.3±0.1 10^9
T_e (Mg IX 368 Å/ Mg VIII 315.0 Å)	7.7±0.2 10^9
T_e (Mg IX 368 Å/ Mg VII 367.7 Å)	7.9±0.1 10^9
T_{max} (DEM)	7 10^5
I (O IV 608.40 Å/ Ne IV 542.07 Å)	7.2±0.9
I (Mg VI 349.17 Å/ Ne VI 562.8 Å)	1.1±0.2
I(Mg VII 367.67 Å/ Ne VII 561.73 Å)	7.9±1.3
A_b (Ne) (21.56 eV)	-0.15
A_b (N) (14.53 eV)	0.
A_b (O) (13.61 eV)	0.
A_b (C) (11.26 eV)	0.1
A_b (S) (10.36 eV)	+0.3
A_b (Si) (8.15 eV)	0.
A_b (Fe) (7.87 eV)	+0.2
A_b (Mg) (7.64 eV)	+0.1
A_b (Ca) (6.11 eV)	+0.4
A_b (Na) (5.14 eV)	+0.2

The DEM of the plume area

The NIS and GIS line intensities were then used to deduce plasma parameters, shown in Table 6.3. A *DEM* analysis of the combined intensities was performed, in order to better describe the thermal structure of the plume and to determine element abundances. A constant pressure of 2 x10^{14} cm^{-3} K was adopted, together with the usual assumptions, described at the beginning of this Chapter.

The results are shown in Figure 6.29 and in Table E.1. The DEM peaks at upper transition region temperatures (Mg VII, Ca X), $T \simeq 7\text{x}10^5$ with a quasi-isothermal distribution at these heights.

In the GIS 4 instrument, a comparison of on-disc and off-limb observations clearly shows the presence of a continuum emission. This emission is mainly hydrogen Lyman continuum. This is obvious from any on-disc GIS observation. On the other hand, off-limb observations show both the absence of this recombination continuum and very little stray light ('background'). The wavelength dependence of this continuum can be used as a temperature diagnostic. In particular, the continuum emission in the GIS 4 wavelength range is particularly sensitive to the DEM values at $T \simeq 3 - 6\text{x}10^4$ K, and can therefore be used to constrain the DEM values at those temperatures.

For this observation, as an exercise, the continuum has been evaluated at three different wavelengths, and compared to the theoretical emissivity, in the DEM analysis, together with the emission lines. The continuum emissivities have been calculated (see *Landi et al.*, 1999b for a description of the method) with photospheric abundances and a constant density $N_{\rm e} = 1\text{x}10^{16}$ cm^{-3} (a different choice of these parameters, however, does not significantly alter the result). The continuum points are displayed in Figure 6.29.

There is good agreement between the DEM values required to explain the observed continuum emission and those required to explain the emission of the 'cooler' lines. It is also interesting to note that the He lines are well represented, with the photospheric abundances. This is not new, as it was pointed out by *Jordan* (1975), and recently confirmed by quiet sun SUMER and CDS observations by *Macpherson and Jordan* (1999). However, it should be noted that these lines are probably not optically thin, nor is all the observed continuum emission true continuum emission. If an absolute (and accurate) measurement of the continuum emission is achieved (considering all the possible instrumental effects), then, since this emission is $\sim N_H^2$, it is possible to directly relate the element abundances to the proton density.

Also note that even assuming that the NIS and GIS intensities could not be used for a DEM analysis, due to lack of co-temporality, if one considers only GIS lines and only NIS lines and derive from them a DEM, obtains the same shaped curve. This DEM should not be considered a typical plume DEM because some effects due to the tilt of the plume may still be present. However, this study was made to investigate the validity of the (few) NIS lines that were used for abundance analysis, by adding the information from the GIS spectra. Table E.1 shows that there is good agreement between most of the lines, at least when lines close in temperature are considered. It is well known that the Fe VIII lines require more atomic physics research. Here it is shown how important they are. In fact, they are among the brightest low-FIP lines that are emitted in the lower corona, and could therefore be used in conjunction with the high-FIP O VI or Ne VI lines for further studies of the FIP effect. It should be noted that in this case too, the lines from the Li-like ions are underestimated or overestimated by large factors, which casts serious doubts on their reliability for use as diagnostic lines.

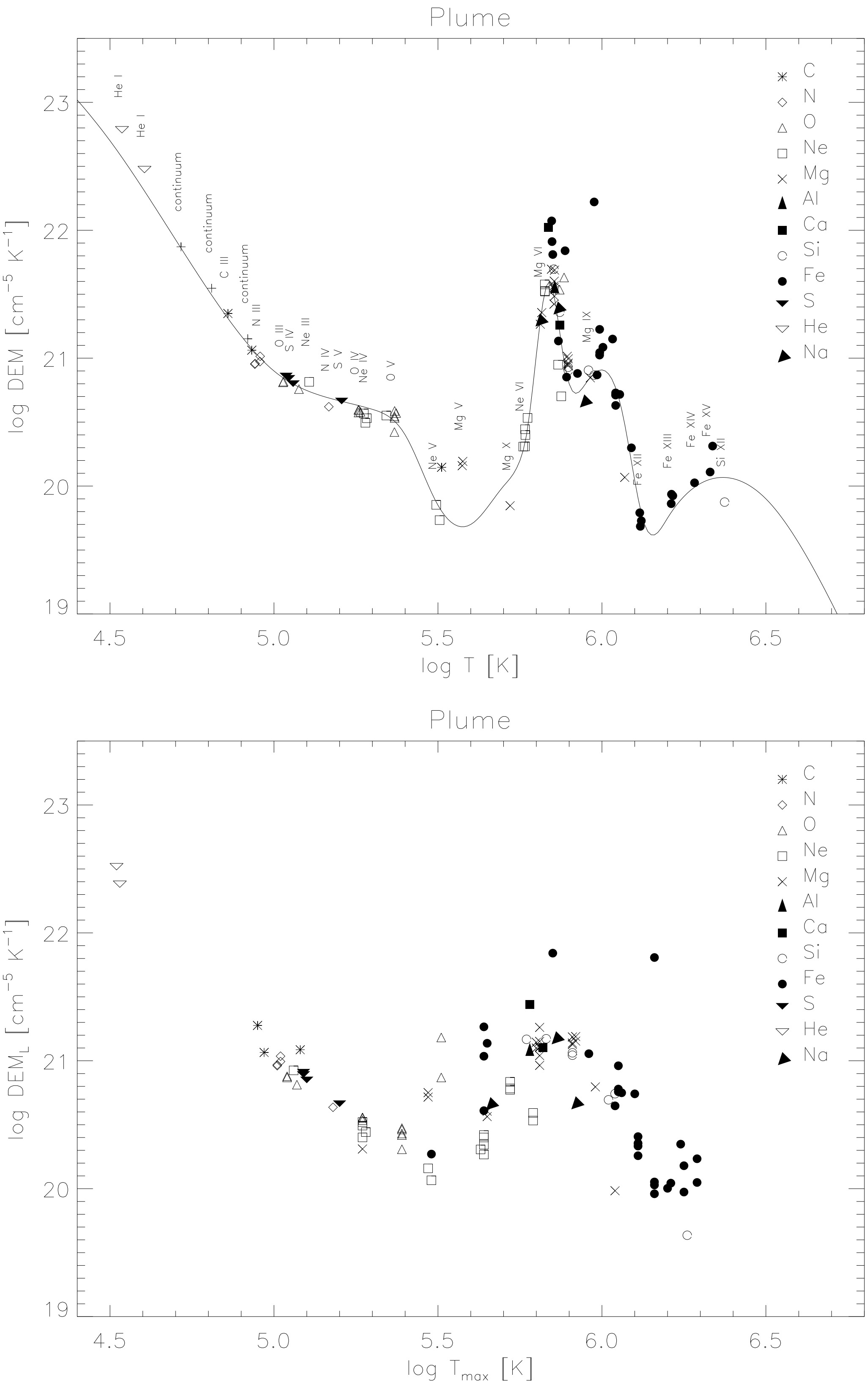

Figure 6.29: *Top: the DEM distribution of the plume area, with the observed points. Bottom: the DEM_L values of the same points. These have been produced using intensities from both GIS and NIS.*

6.3.3 Comparison of GIS spectra with EIT (1997 October 11 data)

The EIT instrument (*Delaboudiniere et al.*, 1995) observes the Sun with four EUV filters, centred around 171, 195, 284, 303 Å. The first two are the principal ones, since the filter at 284 Å has a lower sensitivity, and the filter at 303 Å observes both the chromospheric line He II 303.8 Å and the coronal line Si XI 303.3 Å. The first two filters are referred in the literature as *the Fe IX/X and the Fe XII*, because it is thought that these are the ions that contribute most to the emission. Ratios of images from these two filters have been used by *DeForest et al.* (1997) to estimate that plumes are about 30% cooler than the surrounding coronal hole regions.

In order to confirm this estimate, a comparison between the GIS scan and the EIT 171 Å and 195 Å filters was performed, using EIT images taken almost simultaneously with the GIS spectra on October 11 1997. This was possible because GIS spectrally resolves the emission lines observed by the EIT filters.

Average intensity profiles in the two EIT filters, over the region observed by GIS, were extracted, as shown in Fig. 6.30, where also the ratio of the 195 Å to the 171 Å filter is presented. No intensity calibration factors were applied here, since they are small. This ratio shows a decrease of about 20% from the coronal hole region to the plume region. The observed GIS spectra were then 'filtered' applying the EIT pre-flight filter responses to the CDS spectra (see Fig. 6.31 and Fig. 6.32 for examples on how these filters act on the incident radiation), calculating then the total filtered intensity for each spatial position. The results are shown in Fig. 6.30, with the absolute values arbitrarily scaled. The agreement is quite good, giving confidence in the wavelength-dependence of the pre-flight filter responses.

The GIS intensity ratios of Fe XII 195.1 Å/Fe IX 171.07 Å are also plotted in Fig. 6.30, showing that the *real* intensity ratio is much lower (by a factor of about 0.2) than the value deduced from the EIT filter ratio. Nevertheless, this ratio does decrease (mainly because of the increased Fe IX 171.07 Å intensity) from the coronal hole to the plume, by about 15%, although the spatial position of the minimum is not the same as in the filter ratio curve. This minimum coincides with the peak of the intensity in the line profile.

To see in more detail how the observed EIT intensity changes, depending on the type of solar structure observed, GIS spectra of the two previously selected regions, chosen as representative of coronal hole and plume areas, are plotted in Figs. 6.31 and 6.32, with the same spectra multiplied by the EIT filter response. A quiet sun GIS observation has been added for comparison. The three spectra presented here show how lines, which form at different temperatures, can contribute to the emission seen by EIT.

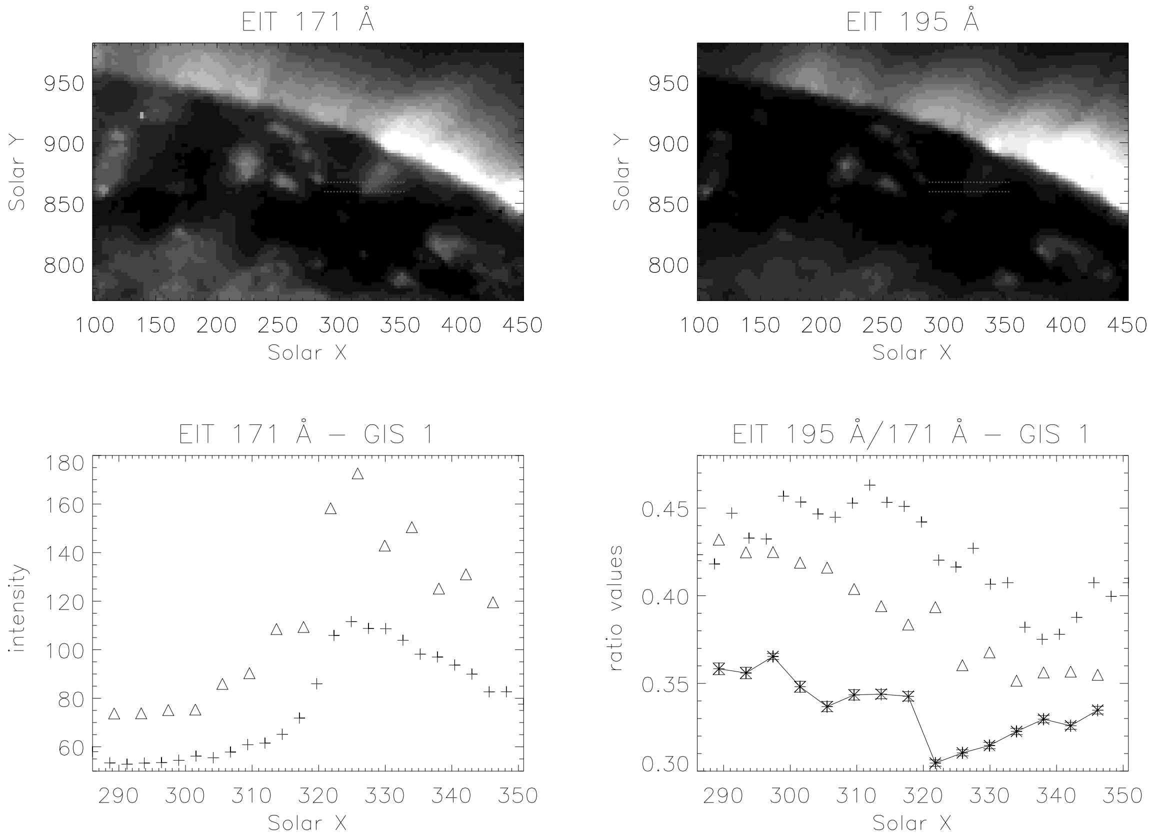

Figure 6.30: *Top: EIT images of the 11th of October 97 (19:00:14 UT – 171 Å; 19:12:30 UT – 195 Å) , with a selected area across the plume overlaid. Bottom left: intensity profiles of the selected area in EIT 171 Å (crosses) with superimposed the observed CDS intensity filtered using the EIT filter response (triangles; intensity in arbitrary units). Bottom right: EIT 195 Å/171 Å intensity ratio (crosses) with the corresponding CDS intensity ratio filtered (triangles) and the intensity ratio of Fe XII 195.1 Å/Fe IX 171.07 Å obtained from CDS (asterisks), shifted by 0.25 for ease of comparison. Note the minimum in the line intensity ratio occurs close to the apparent base of the plume.*

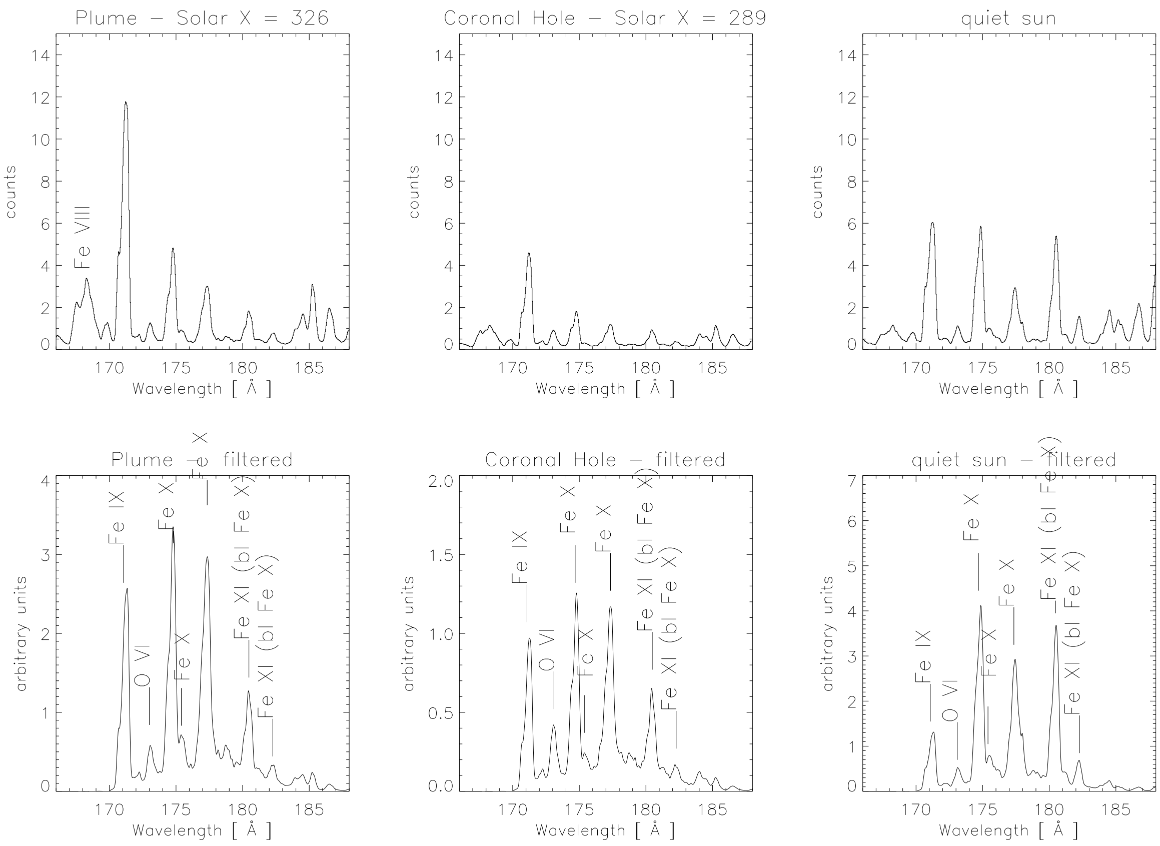

Figure 6.31: *Top: GIS 1 spectra of plume, coronal hole and quiet sun (on the same scale). Bottom: same as above, but multiplied by the EIT 171 Å filter response (scales adjusted separately).*

Considering first the EIT 171 Å filter, Fig. 6.31 shows that in the coronal hole and plume regions the main intensity is from Fe X lines, with some contribution from Fe IX and Fe XI lines, while in the quiet sun spectrum Fe IX 171 Å becomes small. However, the band-pass of the filter includes only emission produced by a restricted temperature range, almost isothermal. In the EIT 195 Å filter, the situation is not quite the same, as Fig.6.32 shows. While in the quiet sun spectrum the main contribution is from Fe XII lines, mixed with some Fe XI and Fe XIII emission, in the coronal hole and plume spectra the cooler lines (Fe VIII, Fe X, Fe XI) become increasingly significant, when compared to the Fe XII lines, as one would expect.

This shows that it is incorrect to assume that the observed emission in the EIT 195 Å filter is always predominantly Fe XII, and explains why plumes are still quite bright in the EIT 195 Å images. In fact, as shown, the emission in the plumes is mainly from low-temperature lines that are visible through the EIT filter. Furthermore, since the lines observed in the EIT 195 Å filter are formed over a wide range of temperatures, it is strictly inappropriate to use this filter for temperature diagnostics. Although not shown

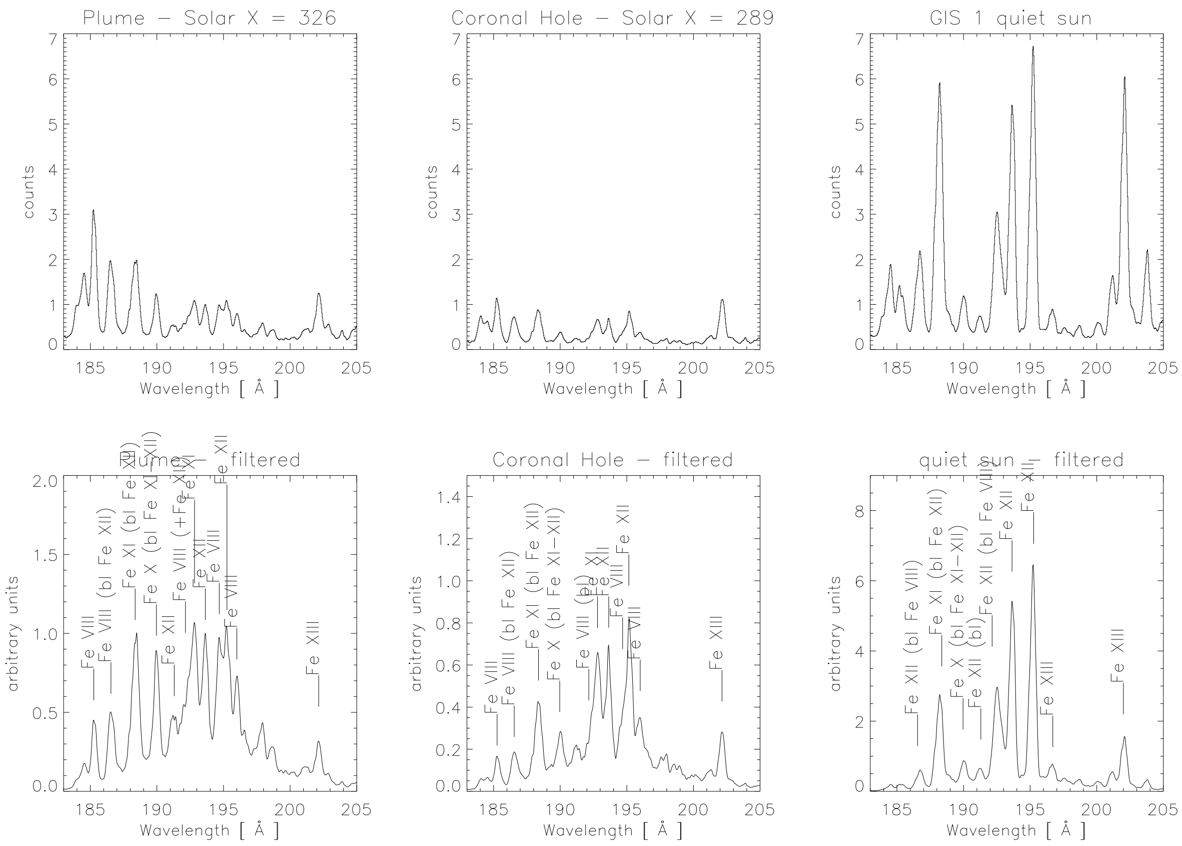

Figure 6.32: *Top: GIS 1 spectra of plume, coronal hole and quiet sun (on the same scale). Bottom: same as above, but multiplied by the EIT 195 Å filter response (scales adjusted separately).*

here, a similar result applies to the EIT 284 Å filter, where the emission is a mix of Fe XV and much cooler lines (Si VII, Mg VII) that are close to this line, as Fig. 6.28 shows.

Finally, it should be stressed that the results shown here are independent of the relative EIT/GIS intensity calibration (which was not a concern here), but only depend on the adopted EIT filter transmission curve, and on the assumption that the plasma characteristics did not change significantly between the GIS and the EIT observation. The latter assumption is reasonable, since all the lines seen in the two filters are coronal and so are not subject to rapid fluctuations. GIS *ghosting*, which becomes non-negligible in the quiet sun observation, does not change the main characteristics of the spectra in this case.